Feasibility study of fluctuations of net-proton, net-charge, and net-kaon multiplicity distributions in the CBM experiment

A Thesis Submitted
in Partial Fulfilment of the Requirements
for the Degree of

MASTER OF SCIENCE

by

DIPTANIL ROY

to the

School of Physical Sciences

National Institute of Science Education and Research

Bhubaneswar

May 14, 2019

DEDICATION

To my sanity.

DECLARATION

I hereby declare that I am the sole author of this thesis in partial fulfillment of the requirements for a postgraduate degree from National Institute of Science Education and Research (NISER). I authorize NISER to lend this thesis to other institutions or individuals for the purpose of scholarly research.

Signature of the Student

Date:

The thesis work reported in the thesis entitled **"Feasibility study of fluctuations of net-proton, net-charge, and net-kaon multiplicity distributions in the CBM experiment"** was carried out under my supervision, in the **School of Physical Sciences** at NISER, Bhubaneswar, India.

Signature of the thesis supervisor

School:

Date:

ACKNOWLEDGEMENTS

This thesis is far from being a product of my creation. As such, this project will be only half done if I do not begin this report by thanking the people who endured my stupidity at every step, eventually pushing me over the line. I start by thanking Dr. Ranbir Singh who had initiated me to the lengthy derivations and made them graspable for me. I thank all the lab members of the Experimental High Energy Physics Group who sat through my presentations and poured in their suggestions. I extend my heartfelt gratitude to Dr. Subhasish Samanta, Sourav Kundu, Ashish Pandav, and Debashish Mallick, without whose immense patience, I would still be debugging my codes on submission date.

I would also like to reach out to my fellow mates in Physics Batch 14 who have often been tremendous supports, knowingly or unknowingly. Knowing that your fellow comrades are as miserable as you is a peace and motivation of another kind, I have realised. Finally, it is only done when I thank Prof. Bedangadas Mohanty, my guide who has given me this opportunity to work with this wonderful group and appreciate research like never before.

ABSTRACT

Fluctuations of conserved quantities are sensitive observables to probe the signature of QCD phase transition and critical point in heavy-ion collisions. With the UrQMD model, we have studied the centrality and energy dependence of various order cumulants (up to fourth order) of net-proton, net-charge and net-kaon multiplicity distributions in Au+Au collisions at lab energies of 4, 6, 8, and 10 AGeV. We further calculated the cumulants after UrQMD events were passed through the CBM detector setup and probed different methods to get back the real cumulants from the data from the detctors. Furthermore, we studied the second order mixed cumulants of the above net-particle distributions as they are also related to quantities which are sensitive to the QCD phase transition. To correct for detector inefficiencies, we used two different methods : binomial acceptance and unfolding, and showed that cumulants of unfolded distributions have better agreement with the real cumulants from UrQMD. Finally, to correct for the mixed cumulants, we introduced unfolding for two-dimensional distributions and successfully corrected for detector inefficiencies.

Contents

List of Figures

List of Tables

Chapter 1

Introduction

The Compressed Baryonic Matter experiment (CBM), planned at Facility for Antiproton and Ion Research (FAIR) in Darmstadt, aims at investigating the nuclear matter phase diagram in the region of high net baryonic densities and moderate temperatures [1]. This is complimentary to the experiments at Large Hardron Collider (LHC) and Relativistic Heavy Ion Collider (RHIC) energies, which explore the Quantum Chromodynamics (QCD) phase diagram in the transition region between quark-gluon-plasma (QGP) and hadron gas, at vanishing baryon chemical potentials, and high temperatures [2]. A schematic of the QCD phase diagram is shown in Fig.1.

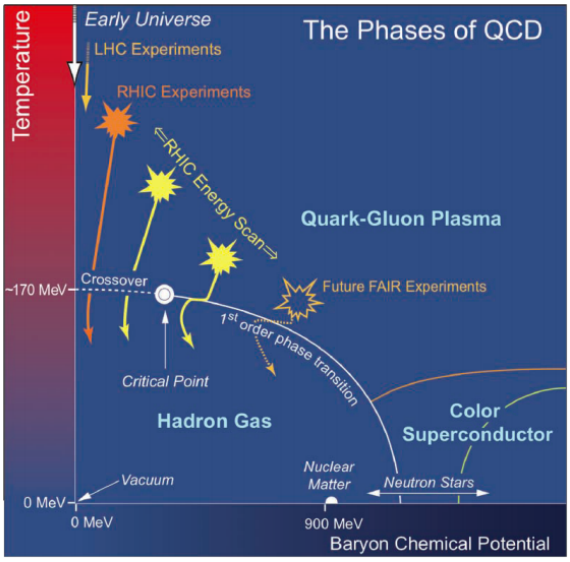

Figure 1.1: Schematic of the QCD Phase Diagram [3].

At $\mu_B = 0$, it has been found theoretically that there occurs a cross-over transition between hadronic and quark-gluon phases at high temperatures [4]. Recent model

calculations have also predicted a QCD critical point (CP) and a first order phase boundary between quark-gluon and hadronic phases at finite μ_B [5]. The experimental discovery of a first order phase transition or a critical point in the QCD phase diagram would significantly enhance our understanding of strong interactions [6, 7], along with the knowledge of neutron stars, and origin of hadron masses. Among the primary goals of the CBM experiment are the search for the predicted first order phase transition between hadronic matter and partonic matter and the search for the critical point.

A good signature of a phase transition and a CP are non-monotonic variations of observables related to the moments of the distributions of conserved charges (α) such as net-baryon (B), net-charge (Q), and net-strangeness (S) number with centre-of-mass energy per nucleon $\sqrt{s_{NN}}$ [8]. One of the primary aims of the Beam Energy Scan (BES) [9, 10] at RHIC was to look at multiplicity distributions of particles which carry these conserved charges ($\alpha = B, Q, S$) and identify the signature of criticality. It is reported that the n-th order cumulants of the net-multiplicity distributions (κ_α^n) are related to the n-th order thermodynamic susceptibilities (χ_α^n) of the corresponding conserved charges in QCD that diverge near the CP [11] -[14]. The cumulants, unlike the thermodynamic susceptibilities, do not diverge near the CP but obtain large finite values, owing to the finite system size and finite time for evolution of the system [15]. Following the BES program, the first measurements of the beam energy ($\sqrt{s_{NN}} = 7.7 - 200$ GeV/c) and collision centrality dependence of the mean(M), standard deviation (σ), skewness(S), and kurtosis (κ) have been reported for net-proton (a proxy for net-baryon) [16], net-charge [17], and net-kaon (a proxy for net-strangeness) [18] multiplicity distributions in Au-Au collisions at midrapidity. These observables have shown a centrality and beam energy dependence for the net-proton distributions, as shown in Fig.1.2, which is neither predicted by non-CP transport

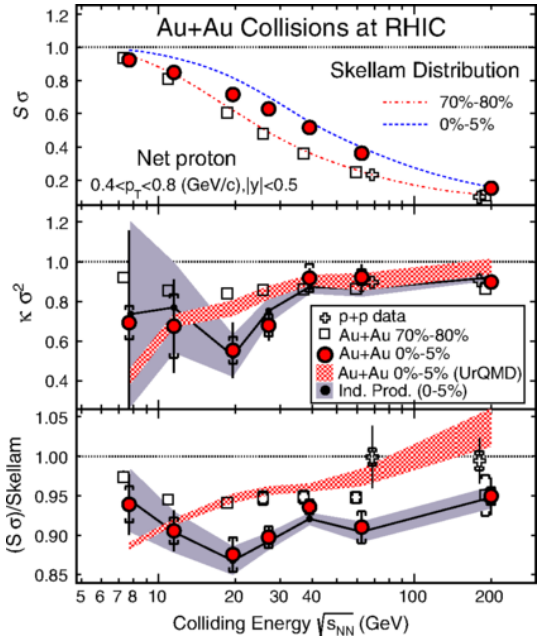

Figure 1.2: Beam Energy Dependence of $S\sigma$, and $\kappa\sigma^2$ for net-proton distributions, after all corrections, for most central (0-5%) and peripheral (70-80%) bins from Au-Au and p-p collisions at RHIC. This is taken from [16].

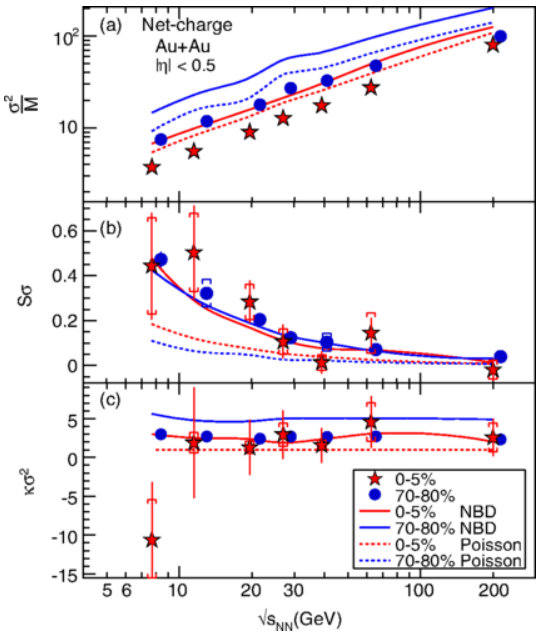

Figure 1.3: Beam Energy Dependence of a)σ^2/M, b)$S\sigma$, and c)$\kappa\sigma^2$ for net-charge distributions, after all corrections, for most central (0-5%) and peripheral (70-80%) bins from Au-Au collisions at RHIC. This is taken from [17].

model (like UrQMD) calculations, nor by the Hadron Resonance Gas Model (HRG). For net-charge and net-kaon distributions, σ^2/M is shown to monotonically increase, while the remaining observables $S\sigma$ and $\kappa\sigma^2$ have a weak dependence of centrality and beam energy, as shown in Figs. 1.3 and 1.4. Within the uncertainties, a smooth behavior had been observed in the products of moments of net-charge as a function of collision energy.

Most measurements, until recently, have focused on the self-correlation of a specific conserved charge (α), which can be quantised by the diagonal cumulants (κ^n_α). Similar to these diagonal cumulants, one can construct and measure off-diagonal cumulants of orders m and n ($\kappa^{m,n}_{\alpha,\beta}$) of the net-baryon, net-charge, and net-strangeness multiplicity distributions [19]. These off-diagonal cumulants are related to the off-

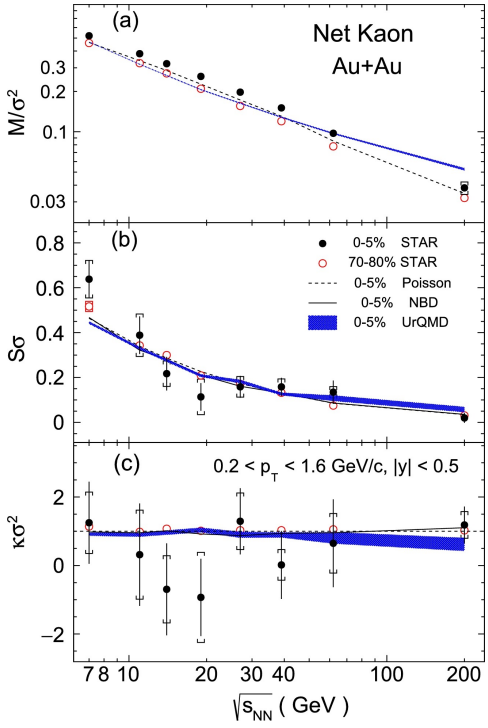

Figure 1.4: Beam Energy Dependence of $S\sigma$, and $\kappa\sigma^2$ for net-kaon distributions, after all corrections, for most central (0-5%) and peripheral (70-80%) bins from Au-Au and p-p collisions at RHIC. This is taken from [18].

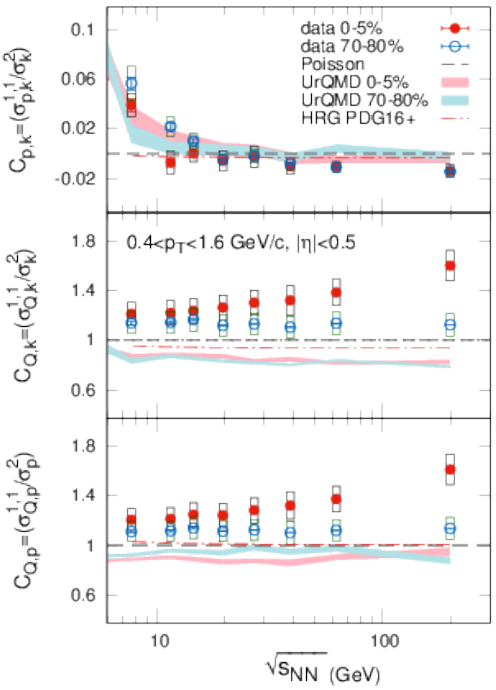

Figure 1.5: Beam energy dependence of cumulant ratios ($C_{p,k}$, $C_{Q,p}$, and $C_{Q,k}$; top to bottom) of net-proton, net-kaon, and net-charge distributions, after all corrections, for most central (0-5%) and peripheral (70-80%) bins from Au-Au collisions at RHIC. This is taken from [19].

diagonal thermodynamic susceptibilities ($\chi^{m,n}_{\alpha,\beta}$) that carry the correlation between different conserved charges (α, β) in QCD [20] - [21]. It has been shown in [20] that baryon-strangeness correlations can be studied by measuring the energy dependence of the ratio of off-diagonal cumulants over diagonal cumulants ($\kappa^{1,1}_{B,S}/\kappa^2_S$), which in turn, is quantified by the susceptibility ratio $C_{B,S} = -3\chi^{1,1}_{B,S}/\chi^2_S$ and is expected to show a rapid change during the transition of the system from de-confined to confined state [22]. The off-diagonal cumulants are also expected to elucidate the character of chromodynamic matter. The mixed susceptibilities (baryon-strange, baryon-charge)

have been reported to differ significantly in the Hadron Resonance Gas (HRG) model and lattice QCD calculations [21, 23]. The off-diagonal cumulants at second-order have also been shown to be sensitive to the difference between calculations from the ideal HRG and lattice QCD [24]. Therefore, measurement of these cumulants of net-multiplicity distributions can put constraints on various models which describe QCD matter [23]. One such study probing the energy dependence of the susceptibility ratios $C_{p,k}$, $C_{Q,p}$, and $C_{Q,k}$, where net-proton (p) and net-kaon (K) serve as proxies for net-baryon and net-strangeness, has been reported recently [19]. As shown in Fig. 1.5, while $C_{p,k}$ has a strong dependence on beam energy and centrality at lower energies, the other observables have strong dependences on centrality and beam energy at all energies, none of which are predicted by UrQMD and HRG. There is, therefore, a need to understand the various processes which contribute to these dependencies. The aim of BES-II in RHIC and CBM experiment in FAIR is to look for the non-monotonic behaviour in these observables by making measurements with high statistical precision. This can then be associated to the existence of a critical point.

The organisation of this thesis is as follows. In Chapter 2, the CBM detector system is briefly described. Then, in Chapter 3, the physics observables related to event-by-event fluctuations are briefly discussed. In Chapter 4, important formulae for the analysis of diagonal and off-diagonal cumulants of net-proton, net-charge, and net-kaon distribution are stated and/or derived. In Chapter 5, the analysis techniques are discussed, and the diagonal and off-diagonal cumulants are presented for net-proton, net-charge, and net-kaon multiplicity distributions. Two different efficiency correction techniques are discussed for the cumulants. Finally, in Chapter 6, the thesis ends with a discussion of the results and the outlook for this analysis.

Chapter 2

The Compressed Baryonic Matter (CBM) Experiment

The Facility for Antiproton and Ion Research (FAIR) is a new accelerator complex currently under construction at the GSI Helmholtz Centre for Heavy Ion Research in Darmstadt, Germany. The Compressed Baryonic Matter experiment [31] is a heavy-ion fixed target experiment, which is being built in FAIR. Heavy nuclei beams will be provided to CBM using two synchrotrons, the SIS100 and the SIS300. The 100 and 300 signifies the bending power ($B.r$) of the magnets used. SIS100 has a strength of 100 Tm, while SIS300 has a strength of 300 Tm. The available kinetic beam energy per nucleon depends essentially on the bending power $B.r$ provided by the dipole magnets.

$$E/A = \sqrt{(0.3 \times B.r \times Z/A)^2 + m^2} - m \tag{2.1}$$

where Z and A are the charge and atomic number of the ion respectively, B is the magnetic field, r is the radius of the synchrotron, and m the mass of the nucleon. Table 2.1 shows the proposed kinetic energy per nucleon for different ion species in SIS100 and SIS300 setup.

The CBM experiment will investigate nucleus-nucleus collisions with energy ranging from 2 AGeV to 45 AGeV in the lab frame [25]. It will complement the BES program of RHIC (where centre of mass energy ranges from 7.7 to 200 GeV per nucleon). The experiment at CBM is fixed-target, designed to run at extremely high interaction rates of upto 10 MHz [26]. It will be capable of measuring both hadrons

Table 2.1: Ion species and their kinetic energy per nucleon for a beam rigidity of 100 Tm at the SIS100 and 300 Tm at the SIS300. The table has been reproduced from [27].

Beam	**Z**	**A**	**E/A GeV SIS100**	**E/A GeV SIS300**
p	1	1	29	89
d	1	2	14	44
Ca	20	40	14	44
Ni	28	58	13.6	42
In	49	115	11.9	37
Au	**79**	**197**	**11**	**35**
U	92	238	10.7	34

and leptons produced in the nuclear collisions. The CBM detector system will accept polar emission angles between 2.5 and 25 degrees and has full azimuthal coverage.

2.1 Detectors in CBM

The setup contains the following sub-detectors :

1. Dipole Magnet [28]: The CBM superconducting dipole magnet is a central part of the detector system. The target station and the Silicon Tracking System (STS) are placed in the magnet gap. The magnet provides a vertical magnetic field with a bending power of 1 Tm.

2. Micro-Vertex Detector (MVD) [29, 30]: The MVD consists of four layers of ultra-thin and highly-granulated monolithic silicon sensors known as Monolithic Active Pixel Sensors (MAPS) which are located close to the target. The four layers are located 5, 10, 15 and 20 cm downstream the target. The MVD is needed to reconstruct the primary collision vertex. It will also detect secondary vertices with high precision which are required for the reconstruction of open charm (D_0, D^* etc.). The angular coverage for MVD is 2.5 deg - 25 deg.

3. Silicon Tracking System (STS) [32]: The STS consists of up to 8 tracking layers of silicon detectors. They are located downstream of the target at distances between 30 and 100 cm in a magnetic dipole field of 1 Tm bending power. The task of the STS is to provide track reconstruction and momentum determination of charged particles. The required momentum resolution is of the order of $\Delta p/p = 1\%$. The angular coverage for STS is 2.5 deg - 25 deg.

4. Ring Imaging Cherenkov Detector (RICH) [33]: The RICH detector comprises a CO_2 radiator and a UV photon detector realized with multi-anode photo-multipliers for electron identification. It is designed to provide identification of electrons and suppression of pions in the momentum range below 8 GeV/c. The angular coverage for RICH is 2.5 deg - 25 deg.

5. Transition Radiation Detector (TRD) [34]: Three Transition Radiation Detector stations each consisting of 34 detector layers will serve for particle tracking and for the identification of electrons and positrons with $p > 1.5$ GeV/c ($\gamma > 1000$). Each layer consists of a radiator where the transition radiation is produced by electrons, and of a gaseous detector in which the deposited energy of charged particles and the transition radiation can be measured. The angular coverage for TRD is 2.7 deg - 44.7 deg.

6. Muon Chamber System (MuCh) [35]: Muons will be measured with an active hadron absorber system consisting of iron layers and muon tracking chambers (MuCh). The final design of the muon detector system consists of 6 hadron absorber layers and 18 gaseous tracking chambers located in triplets behind each absorber slab. The angular coverage for MuCh is 5.7 deg - 25 deg.

7. Time of Flight Detector (TOF) [36]: Charged hadron identification will be

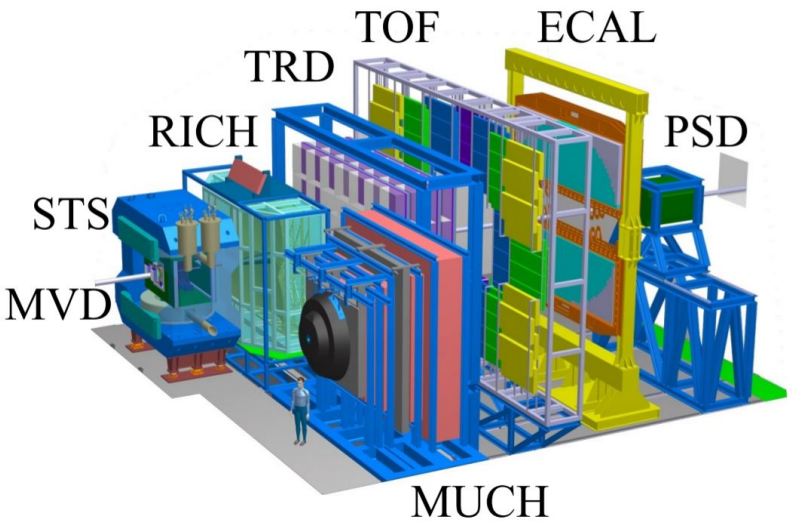

Figure 2.1: The CBM Detector Setup. The components of electron and muon setup are both shown in the diagram.

performed by a time-of-flight (TOF) measurement with a wall of resistive plate chambers (RPC) located at a distance of 10 m behind the target. A micro-strip detector provides the start signal for the TOF measurement. The equations pertaining to the time of flight measurements are derived in Chapter 4. The angular coverage for TOF is 2.5 deg - 25 deg.

8. Electromagnetic Calorimeter (ECAL) and Projectile Spectator Detector (PSD) [37]: ECAL provides information on photons and neutral hadrons in selected regions of phase space. PSD is needed for the determination of the collision centrality and the orientation of the reaction plane.

   CBM will run in two different setups : *Electron setup* and *Muon setup*. The electron setup will comprise of MVD, STS, RICH, TRD, TOF, ECAL, and PSD detectors. In the muon setup, the RICH detector will be replaced by MuCh for muon detection. A summary of the required detectors for different particle measurements is presented in Table 2.2.

Table 2.2: Observables and required detectors. 'x' denotes that the detectors can detect the mentioned observables. The table has been taken from [27].

Observables	**MVD**	**STS**	**RICH**	**MuCh**	**TRD**	**TOF**	**ECAL**	**PSD**
π, K, p		x	x		x	x		x
Hyperons		x			x	x		x
Electrons	x	x	x		x	x		x
Muons		x		x		x		x
Photons							x	x
Photons via $e^{\pm}$ conversion	x	x	x		x	x		x

2.1.1 Detectors used for our analysis

We have used the data from the following detectors for our analysis.

1. **Micro Vertex Detector** for primary collision vertex, and track reconstruction of particles.

2. **Silicon Tracking System** for track reconstruction, and momentum determination of particles.

3. **Time-of-Flight detector** for particle identification.

The Time-of-flight detector is used only for cumulants of net-proton and net-kaon multiplicity distributions, where it is necessary to identify protons and kaons. For analysis of net-charge multiplicity distributions, particle identification is not required, hence data from MVD and STS were only used.

Chapter 3

Event-by-Event Fluctuation Observables

In this thesis, the aim is to look at event-by-event fluctuations of conserved quantities like net baryon number, net charge, and net strangeness, in the CBM detector setup. Theoretically, it has been predicted that at high temperatures, there is a cross-over from hadronic phase to quark-gluon-plasma at $\mu_B = 0$ MeV [4]. At larger μ_B, a first order phase transition is predicted between quark-gluon and hadronic phases, which ends in a critical point (CP). Several other studies have reported that the CP region is unlikely to be found below $\mu_B = 200$ MeV [38].

It has also been observed in several experiments that the value of baryon chemical potential μ_B increases with decreasing center of mass energy $\sqrt{s}$. In fact, the following parameterisation of μ_B vs $\sqrt{s}$ has been reported [39].

$$\mu_B(\sqrt{s}) = \frac{1.308 \text{ GeV}}{1 + 0.273 \text{ GeV}^{-1} \times \sqrt{s}} \tag{3.1}$$

This can be understood by the fact that with increasing $\sqrt{s}$, the amount of entropy (heat) generated grows, while the net baryon number is limited by that of the initial nuclei [40]. The CBM experiment would look for the experimental signatures of a first order phase transition by colliding Au ions at various $\sqrt{s_{NN}}$. The non-monotonic variations of observables which are related to the moments of net baryon, net-charge, and net-strangeness number with respect to the beam energy are predicted to be good signatures of phase transitions and a critical point [20].

3.1 Fluctuations and Correlations

A system in thermal equilibrium in the grand canonical ensemble is characterised by its partition function

$$Z = Tr\left[\exp\left(-\frac{H-\sum_i \mu_i Q_i}{T}\right)\right] \tag{3.2}$$

where H is the Hamiltonian of the system and Q_i and μ_i denote the conserved charges and the corresponding chemical potentials respectively. For our case, these are strangeness, baryon-number, and electric charge. The mean and variances of the partition function are then expressed in terms of the derivatives of the partition function with respect to appropriate chemical potentials.

$$\langle Q_i \rangle = T\frac{\partial}{\partial \mu_i}\log(Z) \tag{3.3}$$

$$\langle \delta Q_i \delta Q_j \rangle = T^2\frac{\partial^2}{\partial \mu_i \partial \mu_j}\log(Z) \equiv VT\chi_{i,j} \tag{3.4}$$

where $\delta Q_i = Q_i - \langle Q_i \rangle$. Here, χ is *susceptibility* defined by

$$\chi_{i,j} = \frac{T}{V}\frac{\partial^2}{\partial \mu_i \partial \mu_j}\log(Z) \tag{3.5}$$

which is generally a measure of (co)-variance. The diagonal susceptibilities, $\chi_{i,i}$, are measures for the fluctuations of the system, whereas the off-diagonal susceptibilities, $\chi_{i,j}$ with $i \neq j$ characterise the correlations between the conserved charges Q_i & Q_j.

Higher order susceptibilities can be defined by differentiating the partition function multiple times with respect to the appropriate chemical potentials

$$\chi_{i,j,k}^{n_i,n_j,n_k} = \frac{1}{VT}\frac{\partial^{n_i}}{\partial(\mu_i/T)^{n_i}}\frac{\partial^{n_j}}{\partial(\mu_j/T)^{n_j}}\frac{\partial^{n_k}}{\partial(\mu_k/T)^{n_k}}\log(Z) \tag{3.6}$$

Higher order cumulants up to sixth order [41] - [45] have been calculated in Lattice QCD, and they provide useful information about the properties of the matter above the critical temperature.

3.1.1 Diagonal Cumulants and Fluctuations

The concept of "fluctuation of conserved quantities" seems contradictory, as for the entire system, none of the conserved quantities will fluctuate. However, by studying a smaller subsystem, we can make sense of the fluctuations of conserved quantities. The small system may exchange conserved quanta with the rest of the system. This is similar to the assumptions which govern a thermal system in the grand-canonical ensemble, discussed above, and Lattice QCD calculations are carried out in this ensemble.

In Lattice QCD, the susceptibilities are expressed in terms of the Taylor coefficients in the expansion of the dimensionless pressure (P/T^4), with respect to normalised chemical potential (μ_i/T). [14]. Here i can represent baryon (B), charge (q), and strangeness (S).

$$P/T^4 = \frac{1}{VT^3}\log[Z(V,T,\mu_i)] \tag{3.7}$$

$$\chi_i^n(T,\mu_i) = \left.\frac{\partial^n(P/T^4)}{\partial(\mu_i/T)^n}\right|_T \tag{3.8}$$

In a grand canonical ensemble, the n^{th} order cumulant of multiplicity distributions are connected to the corresponding susceptibilities by

$$C_{n,i} = VT^3\chi_q^n(T,\mu_i) \tag{3.9}$$

where V denotes the volume of the system. The susceptibilities exhibit singularity near the critical point of the system.

While relating the susceptibilities to the moments, a volume term appears (Eq. 3.9.). This makes it difficult to compare different centralities, and different systems of collisions. However, the ratio of moments like $\frac{C_3}{C_2}$, $\frac{C_4}{C_2}$, are devoid of the volume term, and it has been seen from lattice QCD calculations that these products also change

rapidly near the critical point. Some of the relations are listed below

$$S\sigma = \frac{C_3}{C_2} = \frac{\chi^{(3)}}{\chi^{(2)}} \tag{3.10}$$

$$\kappa\sigma^2 = \frac{C_4}{C_2} = \frac{\chi^{(4)}}{\chi^{(2)}} \tag{3.11}$$

$$\frac{\kappa\sigma}{S} = \frac{C_4}{C_3} = \frac{\chi^{(4)}}{\chi^{(3)}} \tag{3.12}$$

The moments have also been shown to be directly related to the correlation length (ξ) of the system [46]. In finite systems, the correlation length can be at most of the size of the system, therefore, the moments do not diverge near the critical point, instead they take large finite values. Some of the relations are listed below.

$$C_2 \sim V\xi^2 \,|\, C_3 \sim V\xi^{9/2} \,|\, C_4 \sim V\xi^7 \tag{3.13}$$

The most general dependence of moments on correlation lengths is given by $C_n \sim V\xi^{\frac{5}{2}n-3}$ [47]. Hence, the higher moments of distributions of conserved quantities are studied as they have a stronger dependence on ξ.

3.1.2 Off-diagonal Cumulants and Correlations

The correlation between the strangeness S and the baryon B is an useful diagnostic for the presence of string interactions between quarks and antiquarks [20]. To understand this, we consider a situation in which the basic degrees of freedom are weakly interacting quarks and the strangeness is carried exclusively by s and $\bar{s}$. The baryon number they carry is in strict proportion to their strangeness $B_s = -\frac{1}{3}S_s$, thus establishing a strong correlation between strangeness and baryon number. This is in strong contrast to a hadron gas in which the strangeness and baryon number are not so strongly related, at least in high energy regimes. At small baryon chemical potential, for example, the strangeness is carried by kaons which do not possess any baryon number [48]. In lower energies, the situation is more complicated, owing to

the presence of resonances. However, in general, one expects the baryon number and strangeness to be strongly correlated in a quark gluon plasma than in a hadron gas. Such elementary considerations suggest the introduction of the correlation coefficient $C_{B,S}$ [20], given by

$$C_{B,S} = -3\frac{\sigma_{B,S}}{\sigma_S^2} = -3\frac{\langle BS\rangle - \langle B\rangle\langle S\rangle}{\langle S^2\rangle - \langle S\rangle^2} = -3\frac{\langle BS\rangle}{\langle S^2\rangle} \tag{3.14}$$

The last expression makes use of the fact that $\langle S\rangle = 0$. In terms of quark flavours, $C_{B,S}$ can be written as

$$C_{B,S} = -3\frac{\langle BS\rangle}{\langle S^2\rangle} = \frac{\langle (u+d+s)(s)\rangle}{\langle s^2\rangle} = 1 + \frac{\langle us\rangle + \langle ds\rangle}{\langle s^2\rangle} = 1 + \frac{\chi_{us} + \chi_{ds}}{\chi_{ss}} \tag{3.15}$$

,since the baryon number of a quark is $\frac{1}{3}$ and the strangeness of a strange quark is -1. Here, $\langle u\rangle = \langle u - \bar{u}\rangle$ is the average of the net-up-quark number and so on. For uncorrelated quark flavours like in a simple quark-gluon-plasma, we have $\langle us\rangle = \langle ds\rangle = 0$, and hence $\langle C_{B,S}\rangle = 1$.

In contrast, for a gas of uncorrelated hadron resonances, we have

$$C_{B,S} \approx 3\frac{\langle\Lambda\rangle + \langle\bar{\Lambda}\rangle + ... + 3\langle\Omega^-\rangle + 3\langle\bar{\Omega}^+\rangle}{K^0 + \bar{K}^0 + ... + 9\langle\Omega^-\rangle + 9\langle\bar{\Omega}^+\rangle} \tag{3.16}$$

Here, the numerator receives contributions from only strange baryons and anti baryons, while the denominator has contributions from strange mesons too. At the relatively high temperatures, the strange mesons significantly outnumber the strange baryons, so that $C_{B,S}$ is less than 1. As μ_B is increased, the freezeout temperature decreases [49], and consequently strange baryons steadily increase in number as compared to kaons, so $C_{B,S}$ increases [20]. Indeed, at $\mu_B = 0$ and $T_c = 170$ MeV, $C_{B,S} = 0.66$ and at very high μ_B, $C_{B,S} \approx \frac{3}{2}$ [49]. This dependence of $C_{B,S}$ on the hadronic environment is in sharp contrast to the QGP where the correlation coefficient remains one for all temperatures and chemical potentials. Similar behaviour is also expected for charge-strangeness correlations [50].

For $C_{B,Q}$, at low temperatures, the correlation is dominated by protons and antiprotons. Consequently, within the HRG model, it rises exponentially with temperature in this region. In high temperature QCD limit, however, $C_{B,Q}$ vanishes as the quarks effectively become massless with respect to the temperature, and thus, the weighted sum of the charges of up, down and strange quarks vanishes [50]. Thus, model calculations show that these correlations are ideal candidates to probe the transition between the de-confined states of QGP and the confined states of hadrons.

In an experiment however, it is often difficult to capture all baryons. For example, neutrons which are almost equally produced as protons in heavy-ion collisions go completely undetected. It thus stands to question how one can practically measure variations of net baryon number. It has been reported that the proton number susceptibility almost completely reflects the singularity of the baryon number susceptibility near the critical point, and the effect of isospin fluctuations on the shape of net baryon distributions is small [51]. Hence the net proton multiplicity is a good proxy for the net baryon multiplicity.

The same is also true for the measurements of strange particles. It is difficult to perform high-purity event-by-event measurements of neutral strange baryons such as Λ, strange mesons such as K^0_S or other heavy conserved charge carrying particles such as Ω, Σ, Ξ, etc. This is because they require reconstruction using invariant mass spectra that reduces both the efficiency and purity of their detection [52]. Therefore, net-kaon is used as a proxy for net-kaon multiplicity. We also expect that $\kappa^{m,n}_{p,k}$ follows the same trend as $\kappa^{m,n}_{B,S}$, however, it is not correct to simply approximate the latter by the former, without measuring strange-baryons.

In the next chapter, the relevant formulae for the calculations of diagonal and off-diagonal cumulants of net-proton, net-charge, and net-kaon multiplicity distributions are discussed. The different methods of error calculation are also touched upon.

Chapter 4

Important formulae and Derivations

4.1 Kinematic Variables

There are certain kinematic variables which are often used in high energy physics. They are briefly discussed in this section.

1. **Center of mass energy** ($\sqrt{s}$): This is defined as $s = (\mathbf{p_1} + \mathbf{p_2})^2 = (\mathbf{p_3} + \mathbf{p_4})^2$ for a typical 2+2 scattering with particles 1 and 2 incoming, and particles 3 and 4 outgoing, where $\mathbf{p_i}$ denotes the 4-momentum, and m_i is the mass of the i^{th} particle. It reduces to $s = m_1^2 + m_2^2 + 2E_1E_2 - 2\vec{p_1}.\vec{p_2}$, where $\vec{p_i}$ is the 3-momentum, E_i is the energy of the i^{th} particle, and for a fixed target experiment like CBM, since $\vec{p_2} = 0$, it finally takes the form $s = m_1^2 + m_2^2 + 2E_1m_2$. $\sqrt{s}$ is typically a measure of the total 'energy' available in a system.

2. **Minkowski metric**: It is given by $g_{\mu\nu} =$ diag$(1, -1, -1, -1)$.

3. **Transformation matrix**: For our purposes, the incoming beam is taken to be in z-direction, hence the matrix reduces to $\begin{pmatrix} \gamma & -\beta\gamma \\ -\beta\gamma & \gamma \end{pmatrix}$ for the t and z components of the 4-vector only.

4. **Rapidity**: It is defined as follows:

$$y = \frac{1}{2} \ln \frac{E + p_z}{E - p_z} = \frac{1}{2} \ln \frac{1 + \beta}{1 - \beta} \tag{4.1}$$

   Here $\beta = \frac{p}{E}$.

Rapidity is additive under boost from one frame to another, therefore $y_{\text{new}} = y_{\text{old}} + \frac{1}{2}\ln\frac{1+\beta}{1-\beta} = y_{\text{old}} + y_{\text{boost}}$.

5. **Pseudorapidity**: It is defined as follows:

$$\eta = \frac{1}{2}\ln\frac{p + p_z}{p - p_z} \tag{4.2}$$

Using the definition $\cos\theta = \frac{p_Z}{p}$, we have

$$\eta = -\ln(\tan\frac{\theta}{2}) \tag{4.3}$$

When $|\vec{p}| >> m$, $y \approx \eta$.

It is convenient to define rapidity for phenomenological calculations since the mass of the desired particle is known. However, in experiments, it is more convenient to use pseudorapidity as a typical detector or detector component covers some well-defined θ region with respect to the beam axis.

On a side note, for a beam of particles of mass m travelling with kinetic energy E_{kin} in the lab frame, $E_{lab} = E_{kin} + m$ and $p = \sqrt{E_{lab}^2 - m^2}$.

Then, $\beta_{CM} = \frac{p}{E_{lab}+m}$.

4.2 Cumulants

1. **Cumulant generating function** (CGF): For any random variable X, the CGF is defined as $G(t) = \log(< e^{tX} >)$.

2. **Cumulants**: The cumulants are defined by the derivatives of the CGF. The n^{th} order cumulant κ_n is given by

$$\kappa_n = G^n(0) = \left.\frac{\partial^n G(t)}{\partial t^n}\right|_{t=0} \tag{4.4}$$

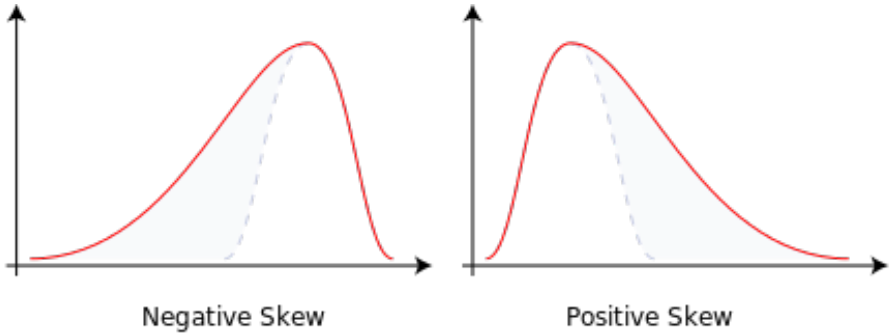

Figure 4.1: Left-skewed and Right-skewed distributions respectively. The image is shared under *Creative Commons License*, and hence is reproduced here [53].

3. **Raw Moments**: The n^{th} order raw moment for a distribution N is defined as $m_n =< N^n >$ where <> denotes the average.

4. **Central Moments**: The n^{th} order central moment for a distribution N is defined as follows:

$$\mu_n = \langle (N - < N >)^n \rangle \tag{4.5}$$

Central moments are related to the n^{th} order cumulants (κ_n) as follows:

$$\kappa_n = \mu_n - \sum_{m=2}^{n-2} \binom{n-1}{m-1} \kappa_m \mu_{n-m} \tag{4.6}$$

For our analysis, we used the relations between raw moments and cumulants for ease of calculation. The cumulants upto 4th order are listed below in terms of raw moments.

$$\begin{aligned} \kappa_1 &= m_1 \\ \kappa_2 &= m_2 - m_1^2 \\ \kappa_3 &= m_3 - 3m_2m_1 + 2m_1^3 \\ \kappa_4 &= m_4 - 4m_3m_1 - 3m_2^2 + 12m_2m_1^2 - 6m_1^4 \end{aligned} \tag{4.7}$$

5. **Variance**: The second central moment (σ^2) is used to describe the width of a distribution.

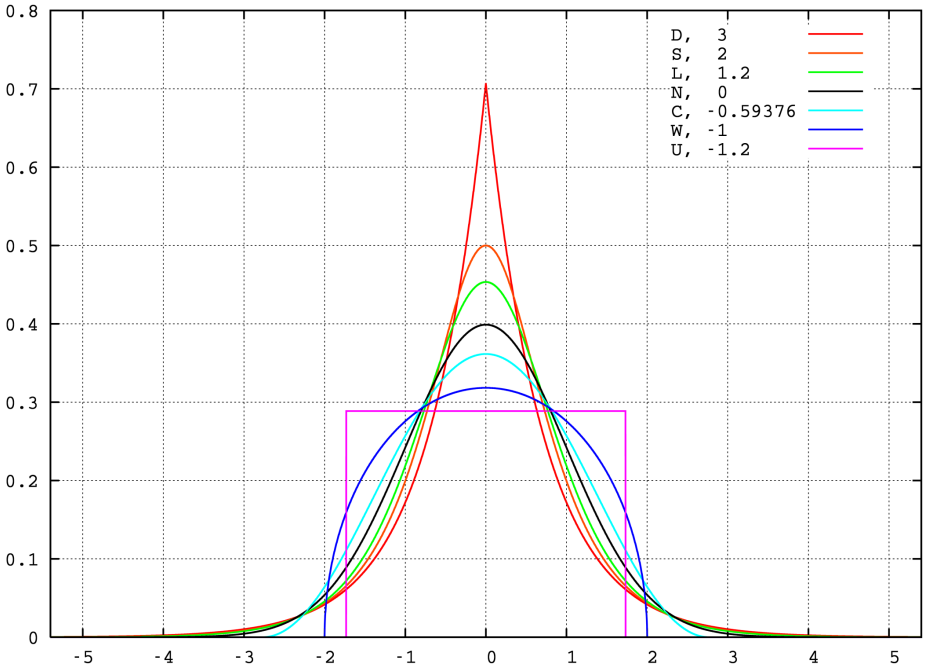

Figure 4.2: Value of Kurtosis for some standard distributions like Laplace Double Exponential, Hyperbolic Secant, Logistic, Normal, Raised Cosine, Wigner Semicircle, and Uniform. The image is shared under *Creative Commons License*, and hence is reproduced here [54].

6. **Skewness**: Skewness, the normalised third central moment, denoted by S, is a measure of the asymmetry of the distribution. It is defined by $S = \frac{\kappa_3}{\kappa_2^{3/2}}$. A distribution can be negative or left skewed if the left tail is longer, and positive or right skewed if the right tail is longer, as shown in Fig. 4.1.

7. **Kurtosis**: Kurtosis, denoted by κ, is a measure of the peakness of the distribution. It is defined by $\kappa = \frac{\kappa_4}{\kappa_2^2}$. A normal distribution has $\kappa = 0$. For any arbitrary distribution, if $\kappa < 0$, it means the distribution produces fewer and less extreme outliers than does the normal distribution. Similarly, if $\kappa > 0$, the distribution produces more outliers than does the normal distribution. Example of the first kind is a *uniform distribution*, while example of the second kind is a *laplace distribution*. Some of these distributions are shown in Fig. 4.2.

8. **Mixed Cumulant**: For two distributions N_α and N_β, we can define the moments by $\delta N_i = N_i - \langle N_i \rangle$ where $i \in (\alpha, \beta)$. Then, the mixed cumulant of order p and q for these two distributions is given by

$$\kappa^{p,q}_{\alpha,\beta} = \langle (\delta N_\alpha)^p \, (\delta N_\beta)^q \rangle \tag{4.8}$$

9. **Properties of Cumulants**:

   9.1. *Translationally invariant*: $\kappa_n(X + c) = \kappa_n(X)$ where X is any random variable and c is any real number.

   9.2. *Homegenous*: $\kappa_n(cX) = c^n \kappa_n(X)$ where X is any random variable and c is any real number.

   9.3. *Additivity*: For independent random variables X and Y,

$$\kappa_n(X + Y) = \kappa_n(X) + \kappa_n(Y) \tag{4.9}$$

10. **Errors on Cumulants**: There are several methods to find out statistical errors in a sample and its related quantities. The most commonly used methods in such analysis are *Bootstrap*, *Delta Theorem*, and *Subgroup Method* [55]. In this analysis, we primarily use "*Delta Theorem*" [56] which provides us with an analytical function to calculate the error.

    Statement of Delta Theorem

    Given a sequence of random variables X_n such that $\sqrt{n}[X_n - \theta] \to N(0, \sigma^2)$ where θ, and σ are finite, and $N(0, \sigma^2)$ represents the standard normal distribution, $\sqrt{n}[g(X_n) - g(\theta)] \to N(0, \sigma^2[g'(\theta)]^2)$, where g is any function for which $g'(\theta)$ exists and is non-zero.

For our case, we can take X_n to be a constant sequence X, and $\theta = \mu$. Then, the statement simplifies to

$$X \sim N(\mu, \frac{\sigma^2}{n}) \implies g(X) \sim N(g(\mu), \frac{\sigma^2}{n}[g'(\mu)]^2) \tag{4.10}$$

To find out the errors, we need to find the variances and covariances of the central moments in the sample ($\hat{\mu}_i$). The general formulae are given in terms of the population central moments (μ_i) below.

$$\begin{aligned} \text{var}(\hat{\mu}_r) &= \frac{1}{n}(\mu_{2r} - \mu_r^2 + r^2\mu_2\mu_{r-1}^2 - 2r\mu_{r-1}\mu_{r+1}) && (4.11) \\ \text{cov}(\hat{\mu}_r, \hat{\mu}_q) &= \frac{1}{n}(\mu_{r+q} - \mu_r\mu_q + rq\mu_2\mu_{r-1}\mu_{q+1} \\ &\quad -r\mu_{r-1}\mu_{q+1} - q\mu_{r+1}\mu_{q-1}) && (4.12) \end{aligned}$$

From Equation 4.11, we have the distribution of sample moment $\hat{\mu}_2$ given by

$$\hat{\mu}_2 = \hat{\sigma}^2 \sim N\Big(\sigma^2, \frac{\mu_4 - \sigma^4}{n}\Big) \tag{4.13}$$

Now, consider the function $g(x) = \sqrt{x}$. Using Delta Theorem on $\hat{\sigma}^2$, we have

$$\hat{\sigma} \sim N\Big(\sigma, \frac{\mu_4 - \sigma^4}{4\sigma^2 n}\Big) \tag{4.14}$$

This gives the variance in μ_2.

$\implies$ **For diagonal cumulants**

Errors in $\kappa_1, \kappa_2, \& \kappa_3$ are trivial and are given by the variances of $\mu_1, \mu_2, \& \mu_3$ respectively. The error in κ_4 is slightly more involved and is discussed below for completeness.

$$\begin{aligned} \kappa_4 &= \mu_4 - 3\mu_2^2 \\ d\kappa_4 &= d\mu_4 - 6\mu_2 d\mu_2 \\ \text{var}(\kappa_4) &= \text{var}(\mu_4) - 12\mu_2\text{cov}(\mu_4, \mu_2) + 36\mu_2^2\text{var}(\mu_2) \end{aligned}$$

$$\implies \text{var}(\kappa_4) = \frac{1}{n}\left(\mu_8 - 12\mu_6\mu_2 - 8\mu_5\mu_3 - \mu_4^2 + 48\mu_4\mu_2^2 + 64\mu_3^2\mu_2 - 36\mu_2^4\right) \tag{4.15}$$

$\implies$ **For off-diagonal cumulants**

For our analysis here, we will only use mixed cumulants of order 2 i.e. $\kappa^{1,1}_{\alpha,\beta}$. For this, we will reduce the mixed cumulant $\kappa^{1,1}_{\alpha,\beta}$ in terms of the variances and covariances of a bivariate distribution of α, β.

$$\begin{aligned} \kappa^{1,1}_{\alpha,\beta} &= \langle (N_\alpha - \langle N_\alpha \rangle)(N_\beta - \langle N_\beta \rangle) \rangle \\ &= \langle N_\alpha N_\beta \rangle - \langle N_\alpha \rangle \langle N_\beta \rangle \end{aligned} \tag{4.16}$$

We define moments for the bivariate distribution of α, β as $\mu_{i,j} = \langle N_\alpha^i N_\beta^j \rangle$.

Then, Eq. 4.16 is given by

$$\kappa^{1,1}_{\alpha,\beta} = \mu_{1,1} - \mu_{1,0}\mu_{0,1} \tag{4.17}$$

To calculate the error, we have to define the variances and the covariances of the moments for this bivariate distribution in the sample $(\hat{\mu}_{i,j})$. They are:

$$\text{var}(\hat{\mu}_{i,j}) = \frac{1}{n}\left(\mu_{2i,2j} - \mu_{i,j}^2\right) \tag{4.18}$$

$$\text{cov}(\hat{\mu}_{i,j}, \hat{\mu}_{k,l}) = \frac{1}{n}\left(\mu_{i+k,j+l} - \mu_{i,j}\mu_{k,l}\right) \tag{4.19}$$

Then, variance of $\kappa^{1,1}_{\alpha,\beta}$ is given by

$$\begin{aligned} \implies \text{var}(\kappa^{1,1}_{\alpha,\beta}) &= \text{var}(\hat{\mu}_{1,1}) + \hat{\mu}_{1,0}^2\text{var}(\hat{\mu}_{0,1}) + \hat{\mu}_{0,1}^2\text{var}(\hat{\mu}_{1,0}) - 2\text{cov}(\hat{\mu}_{1,1}, \hat{\mu}_{0,1})\hat{\mu}_{1,0} \\ &\quad -2\text{cov}(\hat{\mu}_{1,1}, \hat{\mu}_{1,0})\hat{\mu}_{0,1} + 2\text{cov}(\hat{\mu}_{1,0}, \hat{\mu}_{0,1})\hat{\mu}_{1,0}\hat{\mu}_{0,1} \end{aligned} \tag{4.20}$$

Chapter 5

Analysis and Results

5.1 UrQMD Model

UrQMD [57, 58] is an acronym for "Ultra Relativistic Quantum Molecular Dynamics", and was developed at the Frankfurt Institute of Advanced Studies (FIAS), Germany. It is a many-body theory based transport model for simulating heavy ion collisions in the low to medium energy range, like those found in SIS and RHIC. Here a sequence of propagations of particles is simulated numerically, and the inputs include cross sections, the two-body potentials, and decay widths. The UrQMD collision term contains 55 different baryon species (including nucleon, delta and hyperon resonances with masses up to 2.25 GeV/c^2) and 32 different meson species (including strange meson resonances), which are supplemented by their corresponding antiparticle and all isospin-projected states. The states listed can either be produced in string decays, s-channel collisions or resonance decays. For excitations with higher masses than 2 GeV/c^2, a string picture is used. This model allows for an event-by-event analysis of heavy ion reactions similar to the methods which are used for the analysis of experimental data, and hence has been used for this analysis.

5.2 Cumulants from UrQMD at different energies

The net-proton, net-charge, and net-kaon cumulants have been calculated for 4 different energies $E_{lab} = 4, 6, 8, 10$ AGeV from the UrQMD model. The analysis was performed on the HPC clusters located in GSI, Darmstadt, and *Garuda* at NISER.

- **Event Generator :** *UrQMD 3.3*
- **System : Au-Au** collisions ($Z_{Au} = 79$; $A_{Au} = 197$)
- **Impact Parameter :** b $\sim 0 - 14$ fm
- **Energies :** $E_{lab} = 4, 6, 8, 10$ AGeV
- **Number of Events :** ~ 3 million minimum bias

5.2.1 Analysis Cuts

- **Pseudorapidity :** The CBM detector has a pseudorapidity (η) coverage of $1.5 < \eta < 3.8$. Since, we will compare our results from UrQMD to the results from simulation in the CBM setup, we have only chosen particles in this η range.
- **Rapidity :** The particles ((anti)protons and kaons) were chosen in the mid-rapidity region for each energy with a rapidity window of 1. This is varied for different energies as rapidity (y) in the lab frame is dependent on the beam rapidity which changes with beam energy. However, we used the same range for both (anti)protons and kaons as the midrapidity regions for both the species were almost same, as shown in Fig. 5.1.
  - $E_{lab} = 4$ AGeV : $0.68 < y < 1.68$
  - $E_{lab} = 6$ AGeV : $0.85 < y < 1.85$
  - $E_{lab} = 8$ AGeV : $0.98 < y < 1.98$
  - $E_{lab} = 10$ AGeV : $1.1 < y < 2.1$
- **Transverse Momentum :** We have chosen particles having transverse momentum (p_T) within $0.2 < p_T($ GeV/c $) < 2$. The y vs p_T acceptance plots are shown in Figs. 5.2-5.5.

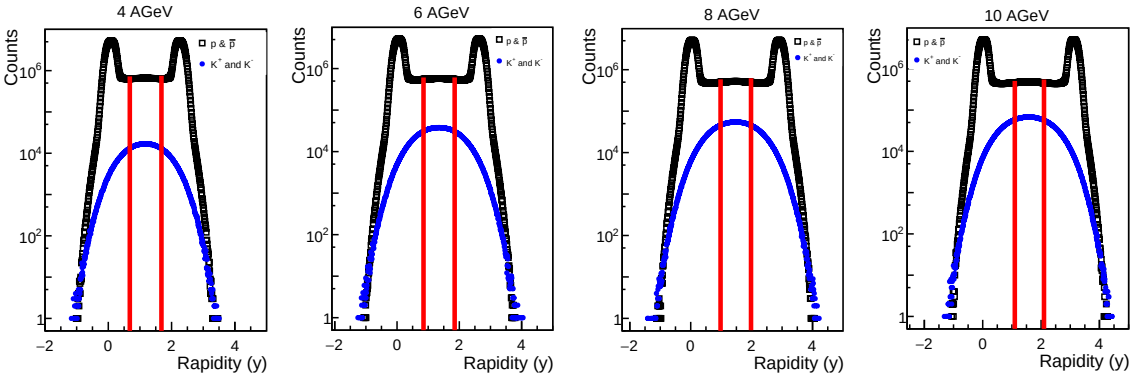

Figure 5.1: Rapidity distributions for (anti)protons and kaons for $E_{lab} = 4, 6, 8, 10$ AGeV. The red lines denote the accepance region at each energy.

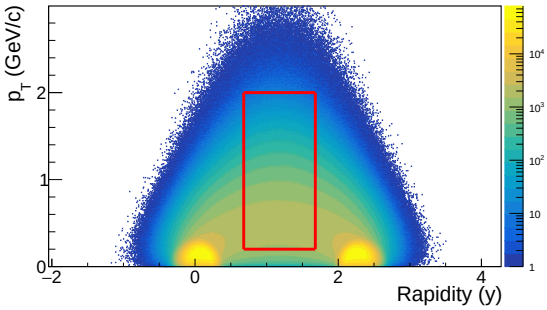

Figure 5.2: Rapidity and p_T acceptance for $E_{lab} = 4$ AGeV.

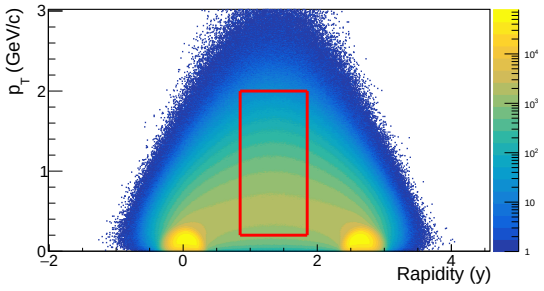

Figure 5.3: Rapidity and p_T acceptance for $E_{lab} = 6$ AGeV.

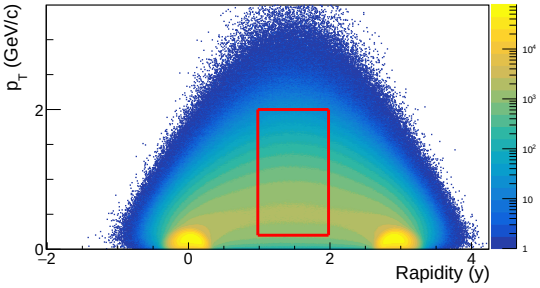

Figure 5.4: Rapidity and p_T acceptance for $E_{lab} = 8$ AGeV.

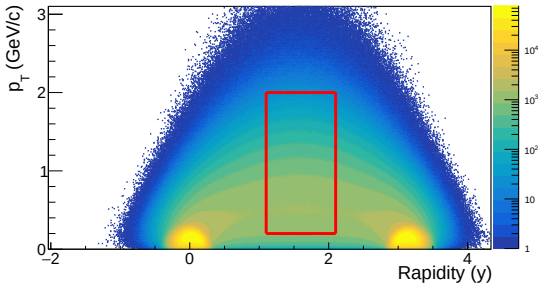

Figure 5.5: Rapidity and p_T acceptance for $E_{lab} = 10$ AGeV

5.2.2 Centrality Selection

Nuclei are extended objects, and hence the volume of the interacting region depends on the impact parameter (b) of the collision. It is defined as the distance between

the centres of the two colliding nuclei. For two nuclei of radii r_1 and r_2, the impact parameter can range from 0 to $r_1 + r_2$. For Au-Au collision, the impact parameter ranges from $0 - 14\ fm$. However, in a real experiment, the impact parameter is not a measurable parameter, hence a new quantity, called centrality is defined based on the impact parameter, and the cross-section of the interaction. The centrality is usually defined as a percentage of the total nuclear interaction cross section σ. The centrality percentile for a $A - A$ collision with an impact parameter b is defined as [59, 60].

$$c(b) = \frac{\int_0^b d\sigma/db'db'}{\int_0^\infty d\sigma/db'db'} \tag{5.1}$$

Since number of particles produced in a collision is directly related to the cross-section, in experiments, centrality classes are defined by the same. The centrality selection is done by the multiplicity of charged particles which is referred as Reference Multiplicity (RefMult). The refmult is chosen differently for each analysis.

5.2.3 Net-Proton Cumulants from UrQMD

RefMult

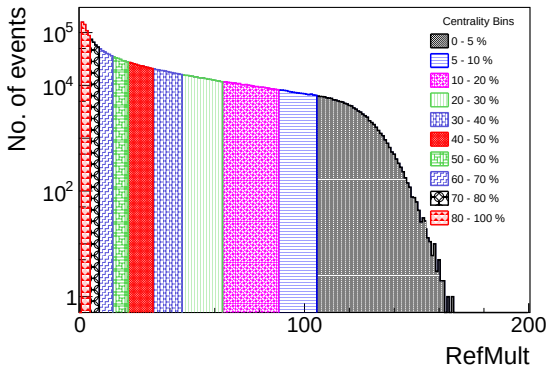

Figure 5.6: Refmult for net-proton cumulants analysis for $E_{lab} = 4$ AGeV.

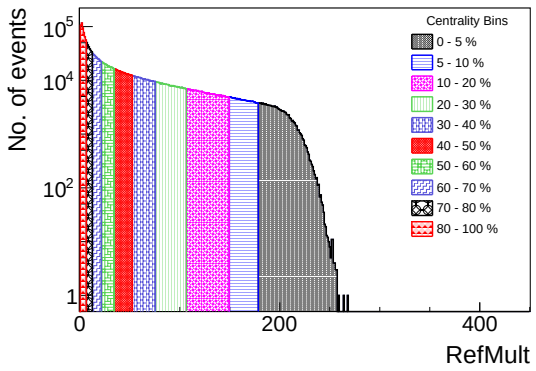

Figure 5.7: Refmult for net-proton cumulants analysis $E_{lab} = 6$ AGeV.

The *RefMult* for net-proton cumulants is shown in Figs. 5.6-5.9. For this analysis, we have used charged pions and kaons within the pseudorapidity acceptance ($1.5 <$

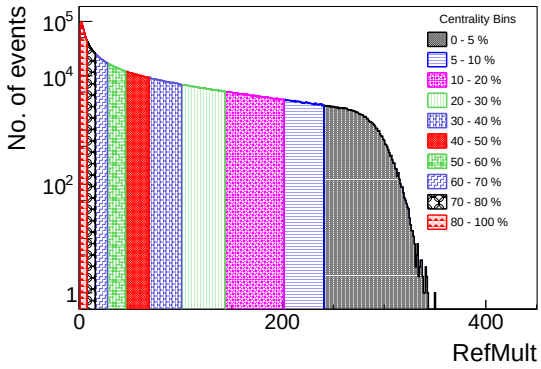

Figure 5.8: Refmult for net-proton cumulants analysis for $E_{lab} = 8$ AGeV.

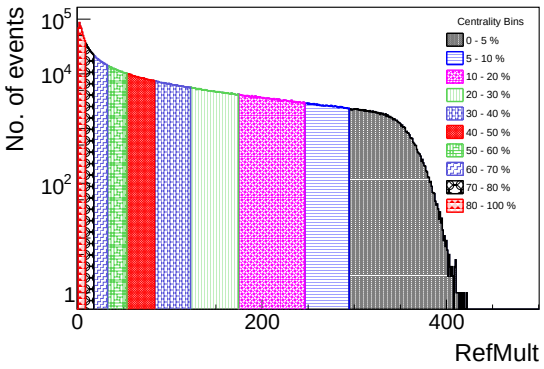

Figure 5.9: Refmult for net-proton cumulants analysis $E_{lab} = 10$ AGeV.

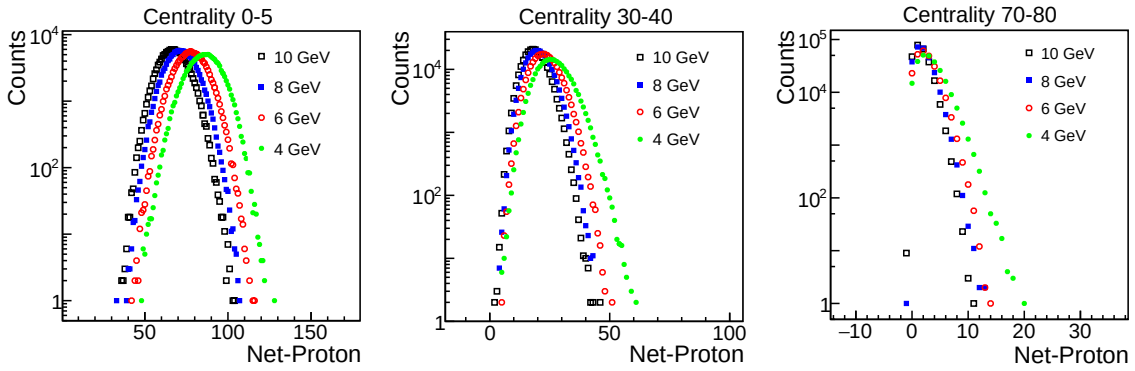

Figure 5.10: Net-Proton multiplicity distributions for 3 centrality classes (0 - 5 %, 30 - 40 %, and 70 - 80 %) for $E_{lab} = 4, 6, 8, 10$ AGeV.

$\eta < 3.8$) to define *RefMult*. This is done to avoid autocorrelation effects. The shaded regions represent the different centrality classes. The net-proton multiplicity distributions for three different centrality classes at different energies have been shown in Fig. 5.10. For these energies, net-proton distribution is dominated by the proton distribution as there are few anti-protons produced. Before we can calculate the cumulants, we have to correct the multiplicity distributions for *Centrality Bin Width Effect* which is discussed below.

Centrality Bin Width Effect

Particle production is dependent on the energy of collision, as well as the centrality. Choosing the finer centrality windows become important so that we can reduce the fluctuations arising due to the selection. The inherent fluctuations arise from the fluctuations in number of participants within the centrality bin. Selection of narrow centrality bins helps to get rid of these fluctuations within a centrality bin. But it may not be always possible to present the results in such narrow bins, mainly because of a lack of statistics. In our analysis, since multiplicity of charged particles is used for centrality selection, the finest bin corresponds to single multiplicity bin. Bin width correction is done by taking the weighted average of the observables [61] in these multiplicity bins.

$$X = \frac{\sum_i n_i X_i}{\sum_i n_i} = \sum_i \omega_i X_i \tag{5.2}$$

where the index i runs over each multiplicity bin, X_i represents the moments or the cumulants in the i^{th} multiplicity bin, n_i represents the number of particles in the i^{th} multiplicity bin, and $\sum_i \omega_i = 1$. All the cumulants in this report have been corrected for this effect. The errors have been calculated using delta theorem [61].

It is also seen from Figs. 5.10 and 5.11 that the average net-proton number for each of these centrality classes decreases with increasing beam energy. This can be explained by the phenomenon called *baryon stopping* where, for lower energies, the initial nucleons slow down to remain at midrapidity region, and thus affect the cumulants. Since this effect is enhanced at lower energies, the first cumulant C_1 shows a decreasing trend with initial energy for all centralities.

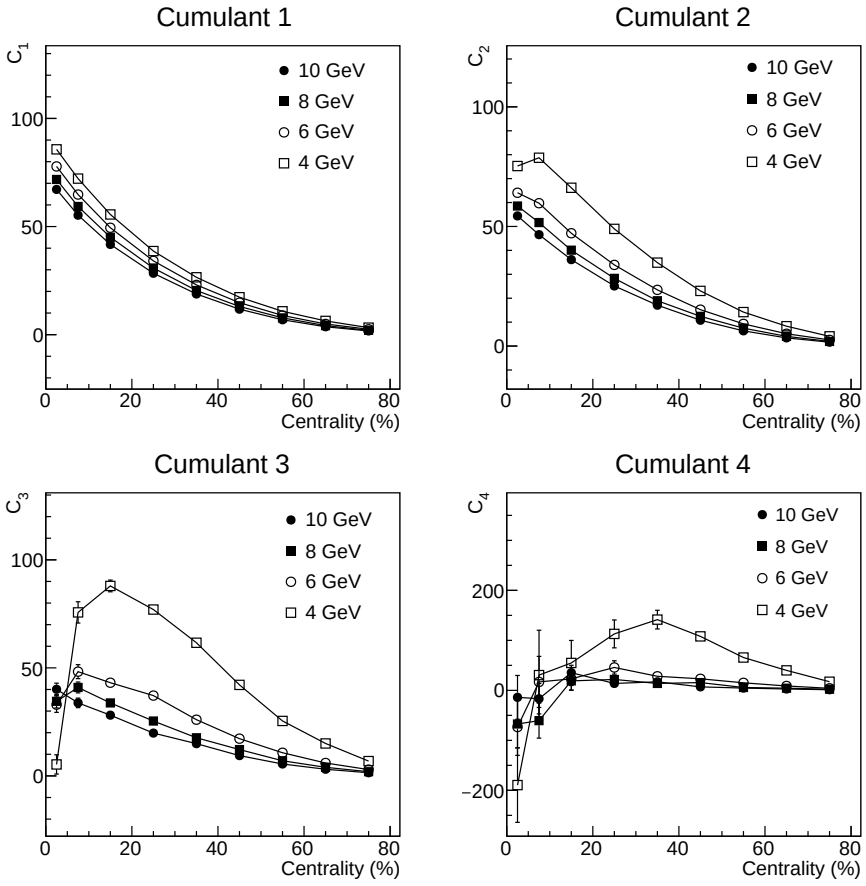

Figure 5.11: The first four cumulants for net-proton multiplicity distributions for $E_{lab} = 4, 6, 8, 10$ AGeV in the η range 1.5 - 3.8, and p_T range 0.2 -2 GeV/c. The rapidity windows for $E_{lab} = 4, 6, 8, 10$ AGeV are 0.68 - 1.68, 0.85 - 1.85, 0.98 - 1.98 and 1.1 - 2.1 respectively. The error bars represent the statistical errors and are within the marker size for some of the cases.

5.2.4 Net-Charge Cumulants from UrQMD

RefMult

The *RefMult* for net-charge cumulants is shown in Figs. 5.12-5.15. To define *RefMult* for this analysis, we have used all charged particles in the pseudorapidity range $1.5 < \eta < 1.8$ & $2.8 < \eta < 3.8$. For analysis, we have used charged particles in the pseudorapidity range $1.8 < \eta < 2.8$. This is done to avoid autocorrelation effects. The net-charge multiplicity distributions for three different centrality classes at different

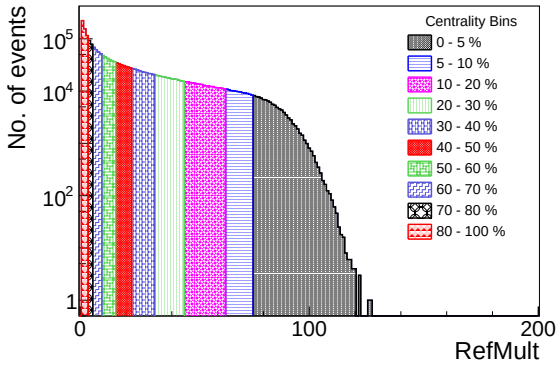

Figure 5.12: Refmult for net-charge cumulants analysis for $E_{lab} = 4$ AGeV.

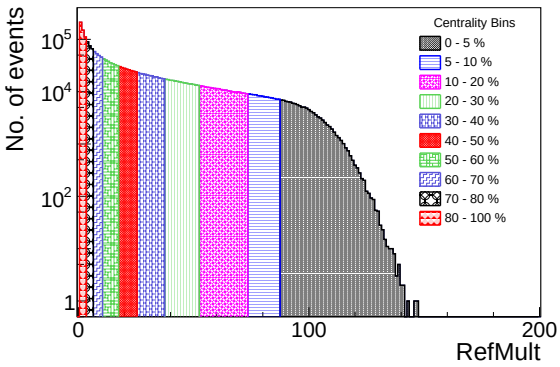

Figure 5.13: Refmult for net-charge cumulants analysis $E_{lab} = 6$ AGeV.

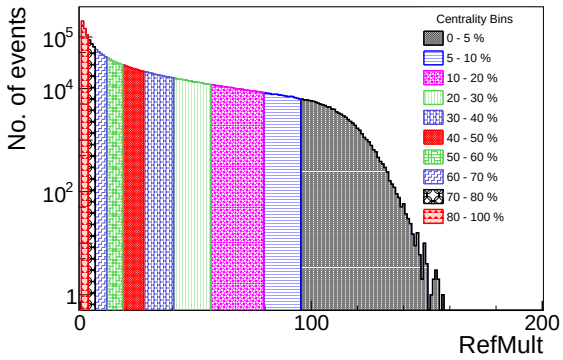

Figure 5.14: Refmult for net-charge cumulants analysis for $E_{lab} = 8$ AGeV.

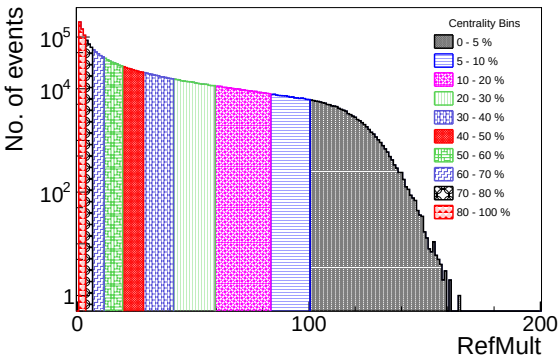

Figure 5.15: Refmult for net-charge cumulants analysis $E_{lab} = 10$ AGeV.

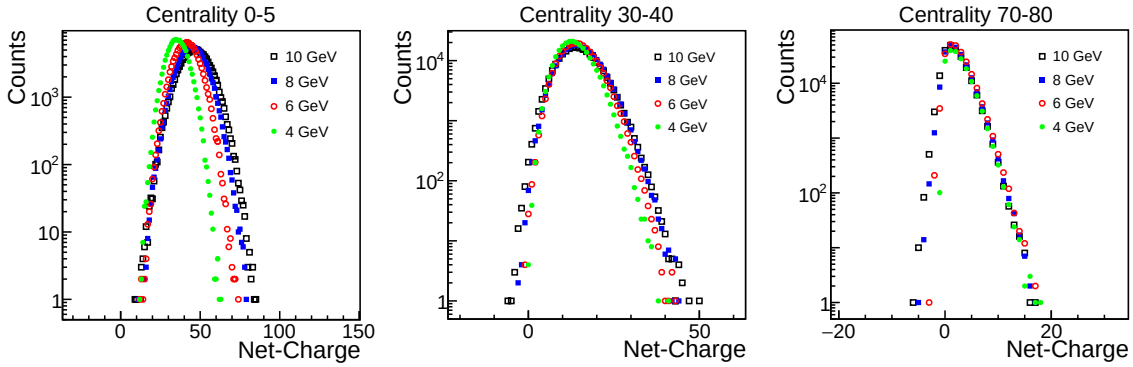

Figure 5.16: Net-Charge multiplicity distributions for 3 centrality classes (0 - 5 %, 30 - 40 %, and 70 - 80 %) for $E_{lab} = 4, 6, 8, 10$ AGeV.

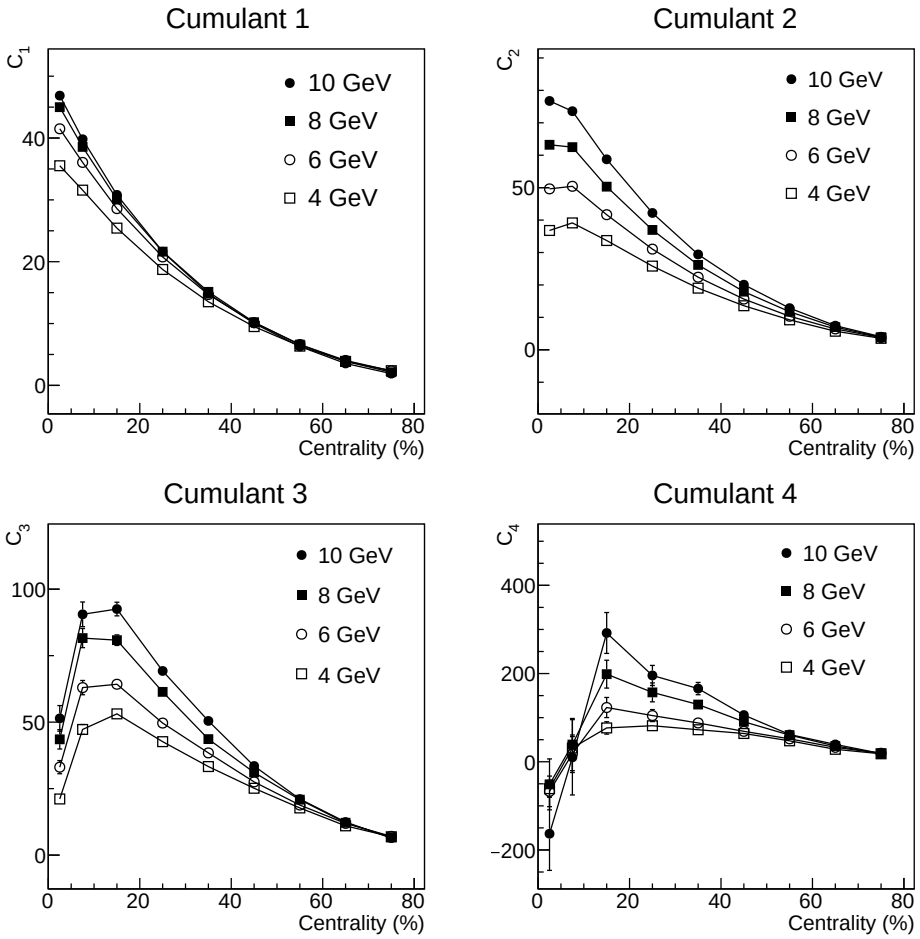

Figure 5.17: The first four cumulants for net-charge multiplicity distributions for $E_{lab} = 4, 6, 8, 10$ AGeV in the η range 1.8 - 2.8, and p_T range 0.2 -2 GeV/c. The error bars represent the statistical errors and are within the marker size for some of the cases.

energies have been shown in Fig. 5.16.

It is also seen from Figs. 5.16 and 5.17 that the average net-charge number for each of these centrality classes increases with increasing beam energy. This can be explained by the fact that, with increasing initial energy, the number of particles produced ($\pi^{\pm}, K^{\pm}$ etc.) increases due to *pair production* and compensates for the decreasing contribution of net-proton to net-charge multiplicity distribution.

5.2.5 Net-Kaon Cumulants from UrQMD

RefMult

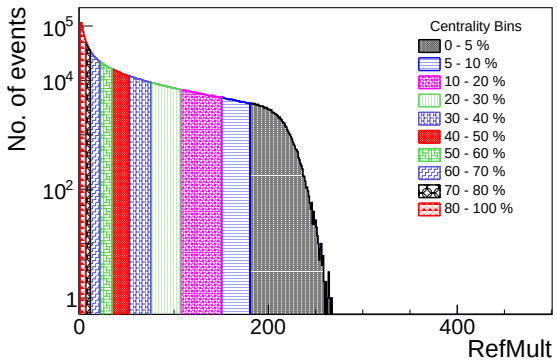

Figure 5.18: Refmult for net-kaon cumulants analysis for $E_{lab} = 4$ AGeV.

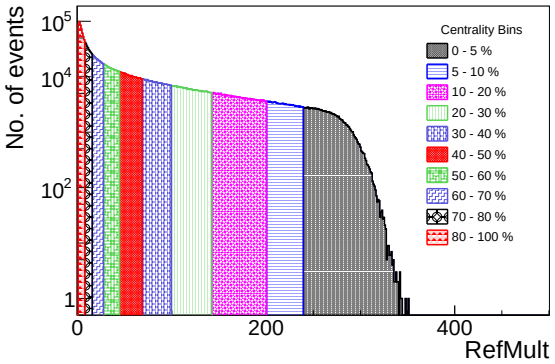

Figure 5.19: Refmult for net-kaon cumulants analysis $E_{lab} = 6$ AGeV.

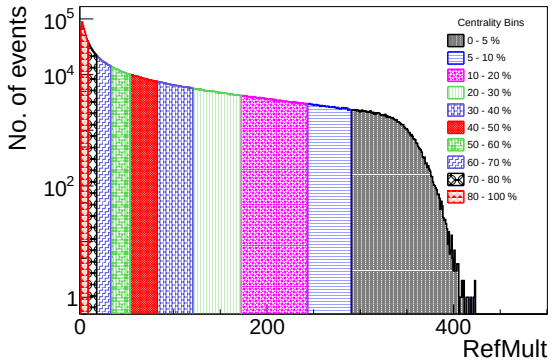

Figure 5.20: Refmult for net-kaon cumulants analysis for $E_{lab} = 8$ AGeV.

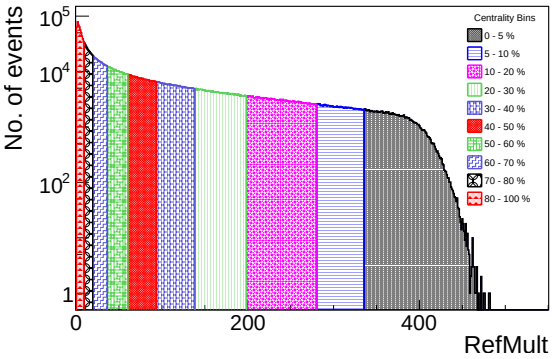

Figure 5.21: Refmult for net-kaon cumulants analysis $E_{lab} = 10$ AGeV.

The *RefMult* for net-kaon cumulants is shown in Figs. 5.18 - 5.21. For this analysis, we have used charged pions, protons and antiprotons in the rapidity acceptance region to define *RefMult*. The particles for the *RefMult* have been chosen in the pseudorapidity acceptance range ($1.5 < \eta < 3.8$). This is done to avoid autocorrelation effects. The net-kaon multiplicity distributions for three different centrality classes at different energies have been shown in Fig. 5.22.

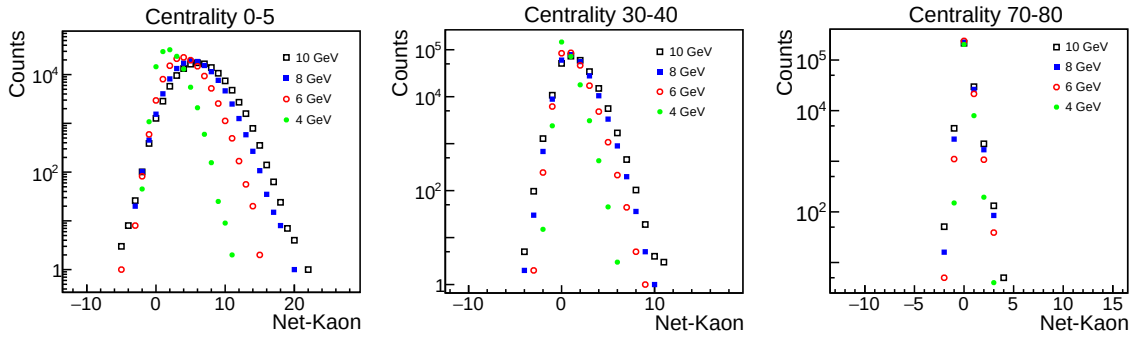

Figure 5.22: Net-Kaon multiplicity distributions for 3 centrality classes (0 - 5 %, 30 - 40 %, and 70 - 80 %) for $E_{lab} = 4, 6, 8, 10$ AGeV.

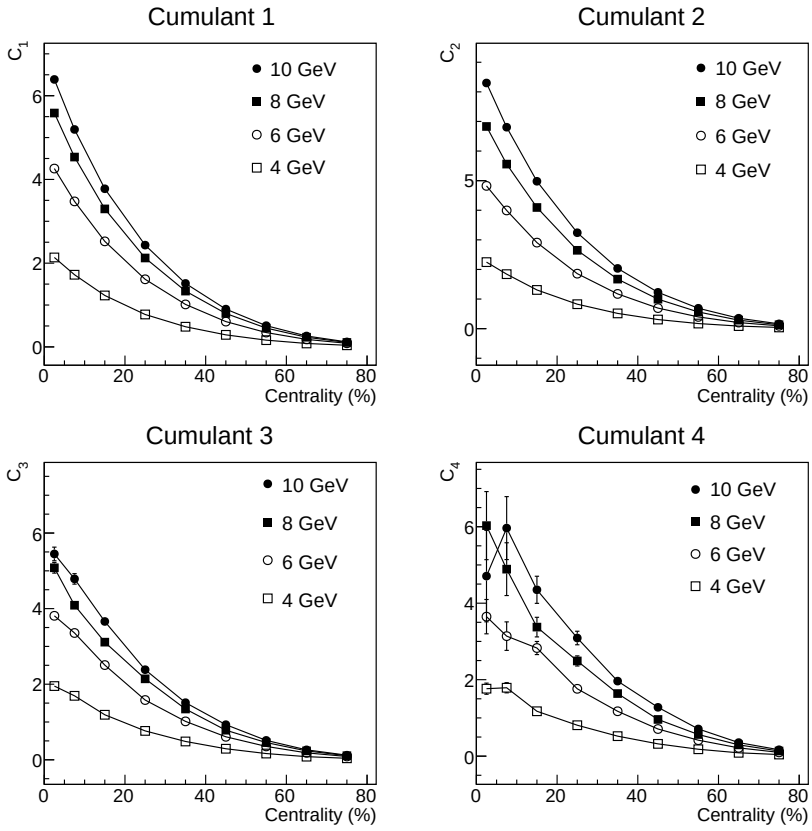

Figure 5.23: The first four cumulants for net-kaon multiplicity distributions for $E_{lab} = 4, 6, 8, 10$ AGeV in the η range 1.5 - 3.8, and p_T range 0.2 -2 GeV/c. The rapidity windows for $E_{lab} = 4, 6, 8, 10$ AGeV are 0.68 - 1.68, 0.85 - 1.85, 0.98 - 1.98 and 1.1 - 2.1 respectively. The error bars represent the statistical errors and are within the marker size for some of the cases.

It is also seen from Figs. 5.22 and 5.23 that the average net-kaon number for each of these centrality classes increases with increasing beam energy. This can be explained by the fact that, with increasing initial energy, the number of kaons produced increases due to *pair production* as there is more energy for creation of new particles. Furthermore, due to the associated production of K^+ with Λ hyperon ($pp \rightarrow p\Lambda(1115)K^+$) [63] which is pertinent at lower energies, the yield of K^+ is greater than the yield of K^-, therefore the average net-kaon number is positive.

5.2.6 Net-Proton and Net-Kaon Mixed Cumulant from UrQMD

RefMult

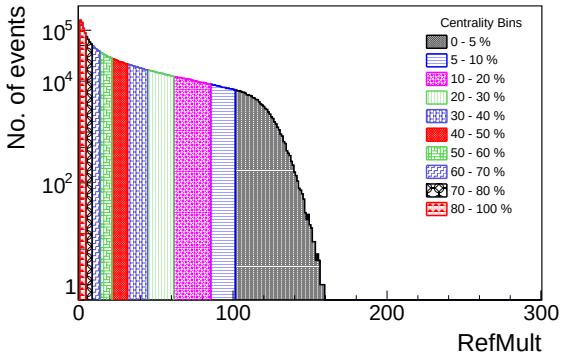

Figure 5.24: Refmult for mixed cumulant analysis for net-proton and net-kaon multiplicity distributions for $E_{lab} = 4$ AGeV.

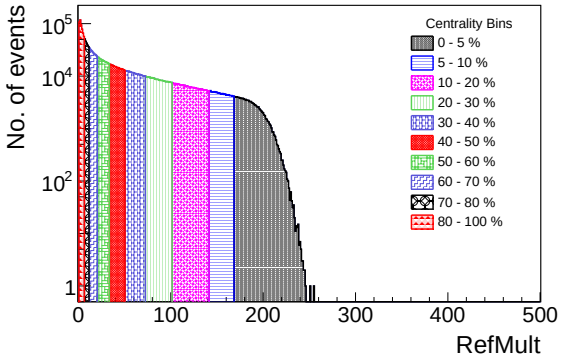

Figure 5.25: Refmult for mixed cumulant analysis for net-proton and net-kaon multiplicity distributions for $E_{lab} = 6$ AGeV.

The *RefMult* for net-proton and net-kaon mixed cumulants is shown in Figs. 5.18-5.21. For this analysis, we have used charged pions within the pseudorapidity acceptance range $1.5 < \eta < 3.8$ to define *RefMult*. This is done to avoid autocorrelation effects.

The mixed cumulant of second order, κ_{pk} is presented in Fig. 5.28. There is an interesting trend in the most central collisions as a function of energy. Firstly, the proton-kaon correlation is enhanced at lower energies and decreases at higher

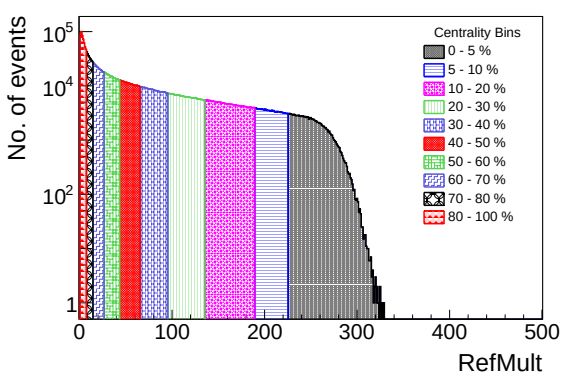

Figure 5.26: Refmult for mixed cumulant analysis for net-proton and net-kaon multiplicity distributions for $E_{lab} = 8$ AGeV.

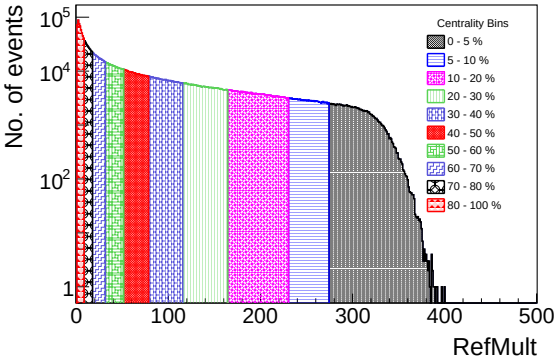

Figure 5.27: Refmult for mixed cumulant analysis for net-proton and net-kaon multiplicity distributions for $E_{lab} = 10$ AGeV.

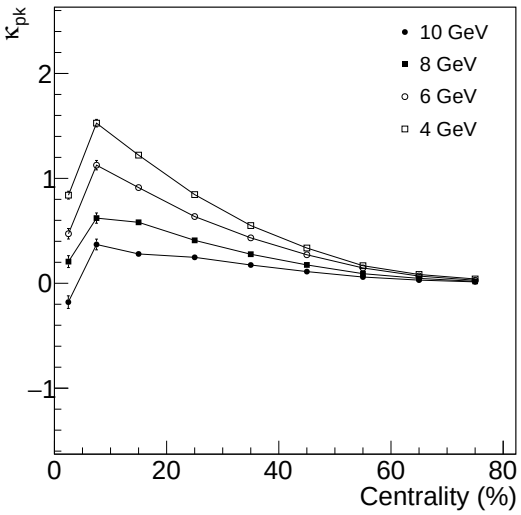

Figure 5.28: Mixed cumulant of second order for net-proton and net-kaon multiplicity distributions for $E_{lab} = 4, 6, 8, 10$ AGeV in the η range 1.5 - 3.8, and p_T range 0.2 -2 GeV/c. The rapidity windows for $E_{lab} = 4, 6, 8, 10$ AGeV are 0.68 - 1.68, 0.85 - 1.85, 0.98 - 1.98 and 1.1 - 2.1 respectively. The error bars represent the statistical errors and are within the marker size for most of the cases.

energies, eventually picking up a small negative value for $E_{lab} = 10$ AGeV. This can be explained by an interplay of two competing effects. The decay of resonance $\Lambda(1520) \rightarrow p + K^-$ with a branching ratio of $(22.5 \pm 0.5\%)$ [64] contributes to the anti-correlation

as such a process increases the net-proton and decreases the net-kaon in the system. This effect is expected to dominate at higher energies, since more energy is available for production of such resonances. Another source of correlation between net-proton and net-kaon arises at lower energies from the associated production process ($pp \rightarrow p\Lambda(1115)K^+$), mentioned earlier. Such a hadronic scattering process dominates owing to the abundance of protons and leads to an increase in the fraction of net-kaon (and also net-lambda) at lower energies [65]. This associated production is followed by the resonance decay $\Lambda \rightarrow p + \pi^-$ with a branching ratio of 63.9%. Since the decay proton from this channel is strongly correlated with the K^+ from the associated production, one expects a further increase in the net-proton to net-kaon correlation as energy decreases. Since UrQMD already includes associated production [66], the energy dependence of the correlation between net-proton and net-kaon can be explained.

5.2.7 Net-Charge and Net-Kaon Mixed Cumulant from UrQMD

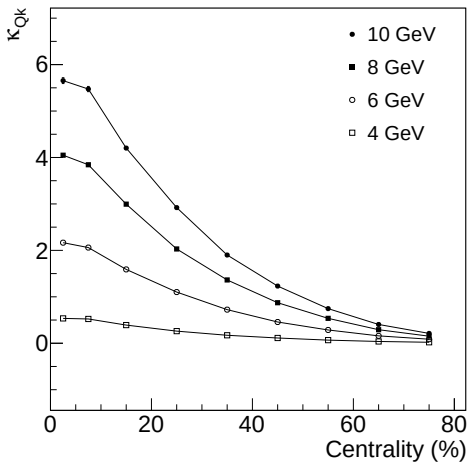

Figure 5.29: Mixed cumulant of second order for net-charge and net-kaon multiplicity distributions for $E_{lab} = 4, 6, 8, 10$ AGeV in the η range 1.8 - 2.8, and p_T range 0.2 -2 GeV/c. The rapidity windows to select kaons for $E_{lab} = 4, 6, 8, 10$ AGeV are 0.68 - 1.68, 0.85 - 1.85, 0.98 - 1.98 and 1.1 - 2.1 respectively. The error bars represent the statistical errors and are within the marker size.

5.2.8 Net-Charge and Net-Proton Mixed Cumulant from UrQMD

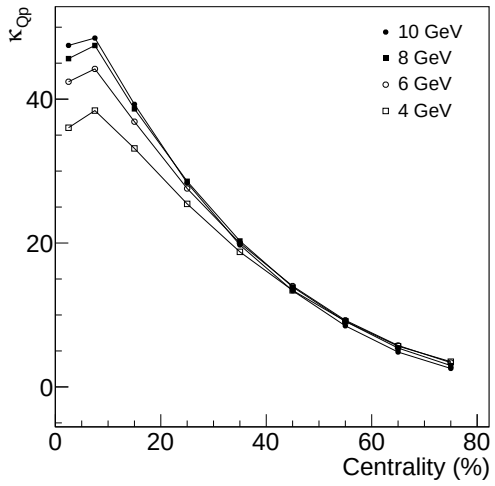

Figure 5.30: Mixed cumulant of second order for net-charge and net-proton multiplicity distributions for $E_{lab} = 4, 6, 8, 10$ AGeV in the η range 1.8 - 2.8, and p_T range 0.2 -2 GeV/c. The rapidity windows to select (anti)protons for $E_{lab} = 4, 6, 8, 10$ AGeV are 0.68 - 1.68, 0.85 - 1.85, 0.98 - 1.98 and 1.1 - 2.1 respectively. The error bars represent the statistical errors and are within the marker size.

The *RefMult* for the analysis of net-charge, net-kaon and net-charge, net-proton correlations are the same as that used in the analysis of the net-charge cumulants, shown in Figs. 5.12-5.15.

The mixed cumulants κ_{Qk} and κ_{Qp} are presented in Figs. 5.29 and 5.30 respectively. Both of these cumulants are significantly larger than κ_{pk}, which can be attributed to the fact that κ_{Qk} and κ_{Qp} has contributions from self-correlations. κ_{pk}, on the other hand, has no trivial self correlations. Both κ_{Qk} and κ_{Qp} show increasing trends with energy. Unlike $\kappa_{p,k}$, many resonances are expected to contribute to κ_{Qk} and κ_{Qp} which might explain why their values increase with energy.

In the following section, we will report the same cumulants from a simulation through the CBM detector setup for $E_{lab} = 10$ AGeV.

5.3 Simulation

We have performed simulation for net-proton, net-charge and net-kaon fluctuations in the CBM framework. The tools used for the simulation are CBMROOT, FairSoft, and FairRoot [67]. The Monte-Carlo generator used for generating the events is Ultra-Relativistic Quantum Molecular Dynamics (UrQMD) [57, 58]. For our analysis, **UrQMD v3.3** has been used. UrQMD produces the data in ASCII format, which is then converted to a "*.root*" file using the sofware UNIGEN (United Generators). This file serves as the input to CBM detector setup in GEANT. The simulation chain is as follows.

The UrQMD data file is passed through the CBM detector setup in GEANT, using the routine '*run_mc.C*, and a root file containing the detector response, generated using monte-carlo methods is the output. The output file, which we name as '*mc.root*' is used as an input to the routine '*run_reco.C*' for reconstructing the tracks. The output file after reconstruction, named as '*reco.root*' is finally used for the analysis. Fig 5.32 shows a typical event display simulated for $Au - Au$ collision at $E_{lab} = 10$ AGeV.

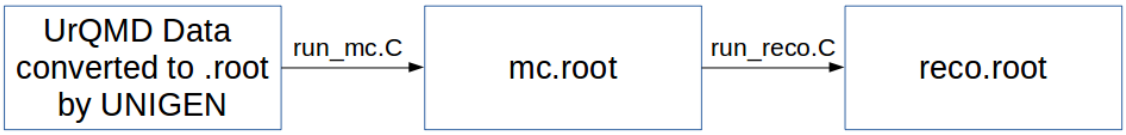

Figure 5.31: Block diagram of the simulation chain for the analysis.

5.3.1 Analysis Tools

The analysis has been done using CBMROOT and some associated softwares which are listed below. The CBM electron setup for SIS100 energies has been used as the

detector setup for this analysis. The SIS100 electron setup consists of MVD, STS, RICH, TRD, and TOF detectors. Nearly 3 million events of Au-Au collisions at $E_{lab} = 10\ AGeV$ have been used for the analysis. The entire simulation and analysis was performed on the HPC cluster located in GSI, Darmstadt. Some important details about the analysis tools are listed below:

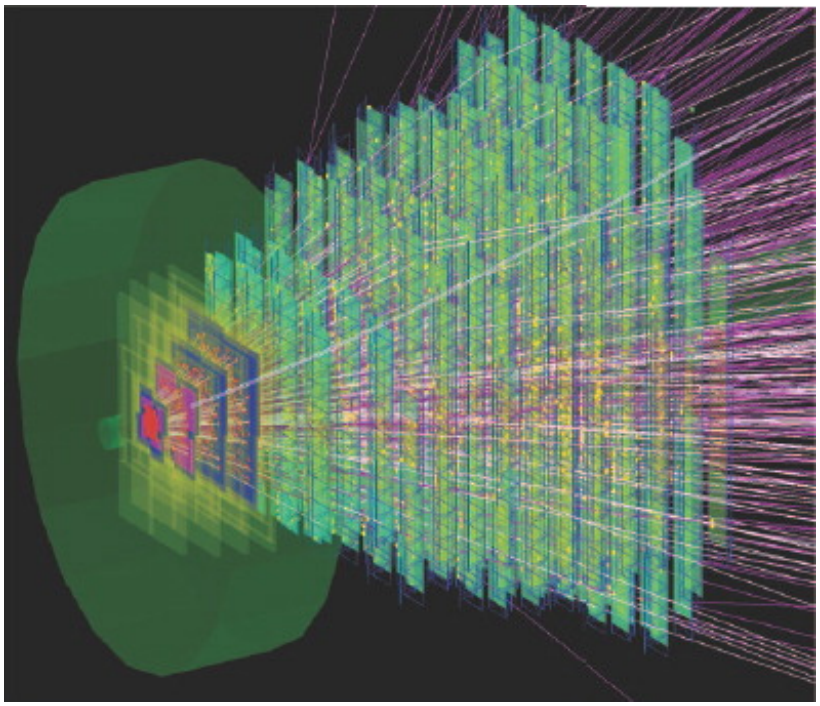

Figure 5.32: Simulation of a central collision of two gold nuclei at a beam energy of 10A GeV. This figure has been reproduced from [68].

1. **Event Generator** : *UrQMD 3.3*

2. **Versions of CBMROOT & associated software**

   2.1. CBMROOT - **MAY2018**

   2.2. FairSoft - **Mar17**

   2.3. FairRoot - **v-17.03a**

3. **Detector Setup**: ***sis100_electron***.

4. **System**: **Au-Au** collisions ($Z_{Au} = 79$; $A_{Au} = 197$)

5. **Impact Parameter**: $b \sim 0 - 14fm$

6. **Energy**: $E_{lab} = 10$ AGeV $\implies \sqrt{s_{NN}} = 4.72$ GeV.

7. **Number of events**: ~ 3 million minimum bias

5.3.2 Analysis Cuts

To select the charged particle tracks with better reconstruction, and to avoid secondaries, various cuts are applied. These cuts are common for the cumulants of all the distributions.

1. **Hits in STS**: The STS detector has 8 consecutive panels, located along the beam axis. To ensure that the momentum of the track is correctly estimated, we have chosen tracks which have more than 6 hits in the STS detector system. This is shown in Fig 5.33.

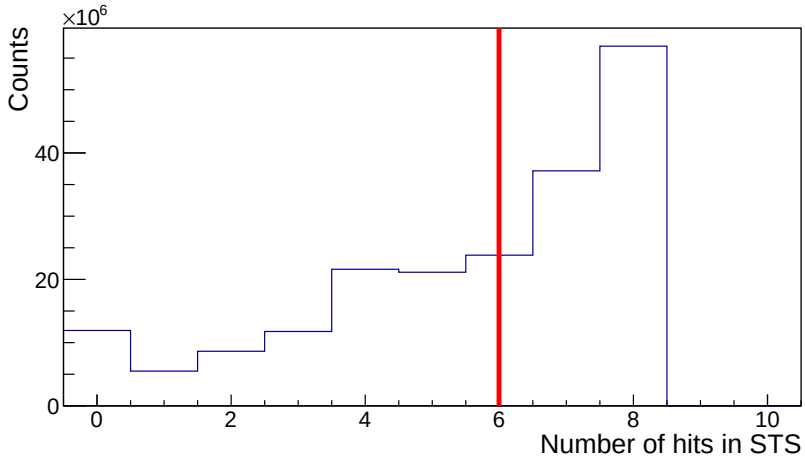

Figure 5.33: The distribution of number of hits in STS detector. Tracks having more than 6 hits out of 8 in the detector have been selected for analysis.

2. **Hits in MVD**: The MVD detector has 4 consecutive panels, located along the beam axis. Along with STS, MVD helps in reconstructing the track vertex. We have chosen tracks which have a minimum of 2 hits in the MVD detector system. This is shown in Fig. 5.34.

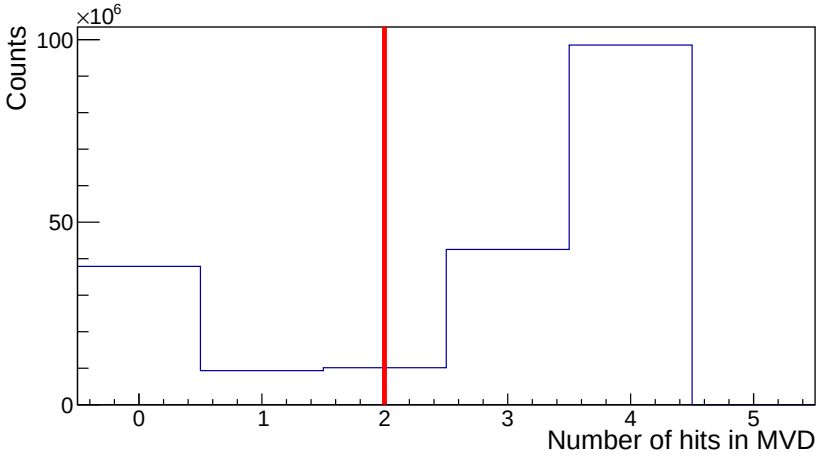

Figure 5.34: The distribution of number of hits in MVD detector. Tracks having more than 2 hits out of 4 in the detector have been selected for analysis.

3. **Distance of Closest Approach (DCA)**: The position of every collision (in cartesian coordinates) is recorded by MVD and STS. After reconstruction, every track is also assigned a position, which denotes the point where it originated. All primary tracks in an event should essentially originate from the event vertex. Distance of closest approach, or DCA refers to the minimum distance of a track from the vertex of the event they belong to. For our analysis, we have selected tracks for which the z-component of the DCA (dca_z) is less than 0.2 cm, and the transverse component ($dca_t = \sqrt{dca_x^2 + dca_y^2}$) is less than 1 cm. as shown in Fig. 5.35. This helps us in getting rid of secondary tracks.

4. **Pseudorapidity**: The CBM detector setup has a polar angle coverage of 2.5 deg to 25 deg. Using Equation 4.3, we thus have set a limit of $\eta \simeq 1.5$ corresponding

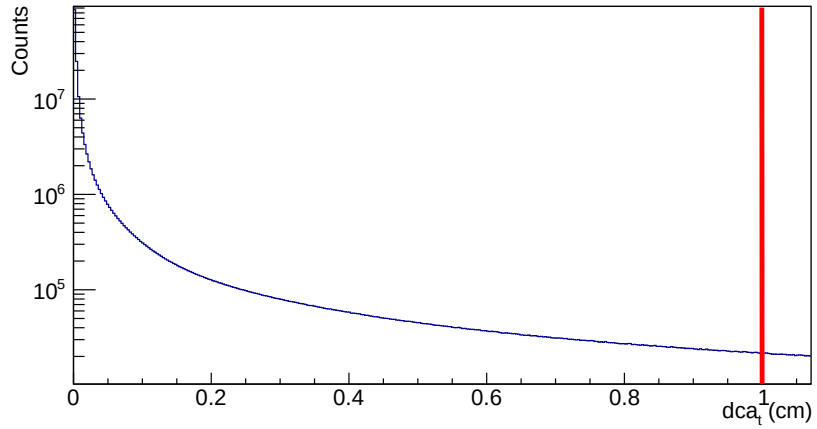

Figure 5.35: The distance of closest approach in transverse plane (dca_t). A dca_t cut is applied at 1 cm ($dca_t < 1$ cm).

to $\theta = 25\,\text{deg}$ and $\eta \simeq 3.8$ corresponding to $\theta = 2.5\,\text{deg}$, as shown in Fig. 5.36.

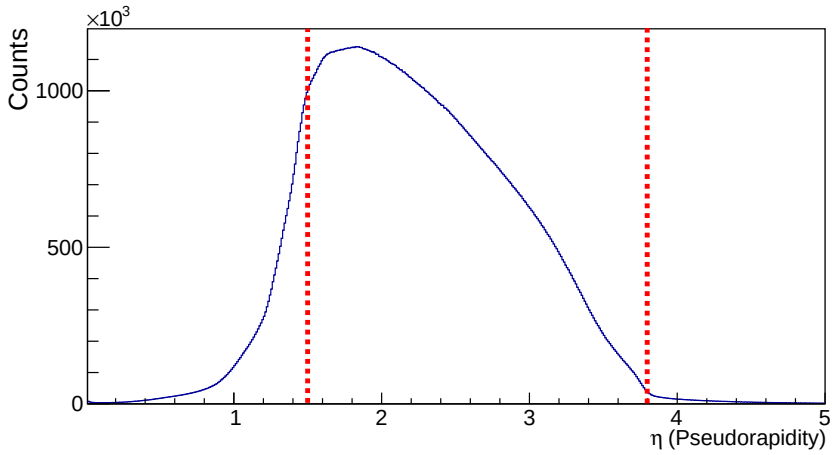

Figure 5.36: The pseudorapidity distribution of all charged particles. The particles in the region $1.5 < \eta < 3.8$ have been chosen for analysis, based on the coverage of the detector.

5. **Hits in TOF**: The Time-of-Flight detector is further downstream as compared to the STS and MVD. Since we have to identify protons, antiprotons and kaons in this analysis, we have only chosen tracks that have at least one hit in TOF.

5.3.3 Net-Proton Fluctuations

Particle Identification

Particle identification in CBM is done using time-of-flight measurements available from the TOF detector. TOF records the length(l) a track has covered before it is detected in TOF, and the time taken (t_{flight}) to reach the TOF detector from the micro-strip detector which measures the start time near the vertex.

$$\beta = \frac{l}{t_{flight}} = \frac{p}{E} \tag{5.3}$$

$$\beta = \frac{p}{\sqrt{p^2 + m^2}}$$

$$\therefore m^2 = p^2\left(1 - \frac{1}{\beta^2}\right) \tag{5.4}$$

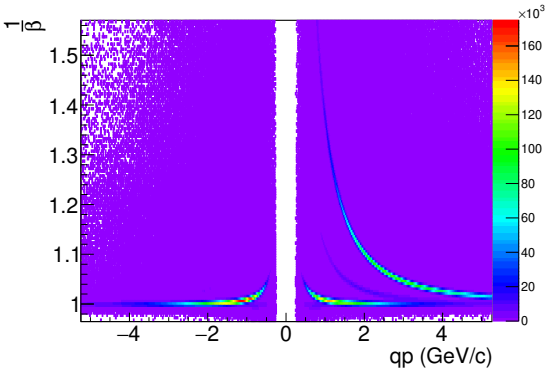

Figure 5.37: $\frac{1}{\beta}$ vs momentum multiplied by charge. The three bands on the positive axis (from bottom) belong to π^+, K^+, and protons respectively. The two bands on the negative axis (from bottom) belong to π^- and K^- respectively. There are very few antiprotons produced at $E_{lab} = 10$ AGeV, as is clearly seen from the absence of a band opposite to that of protons.

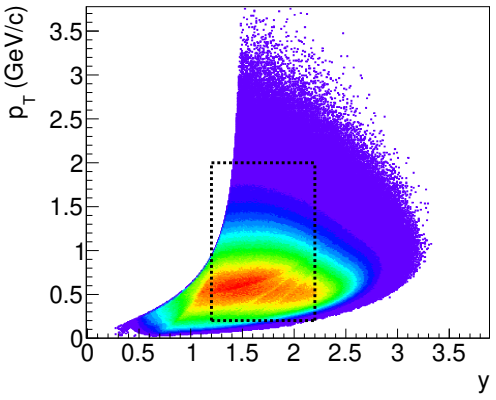

Figure 5.38: Transverse momentum (p_T) vs Rapidity(y) for (anti)protons. In this analysis, we have chosen (anti)protons in the region $1.1 < y < 2.1$ in the rapidity range and $0.2 < p_T < 2.0$ GeV/c in the momentum range, shown by the rectangular region.

Equations 5.3 and 5.4, in conjunction, give the m^2 which we use to identify the particle species. Fig. 5.37 shows $1/\beta$ vs momentum multiplied by charge ($q * p$) for

charged hadrons in Au-Au collision at $E_{lab} = 10$ AGeV. The bands correspond to π, K and protons (from bottom) respectively, and are well separated for $p < 3$ GeV/c. In top panel of Fig. 5.39, m^2 is plotted as a function of momentum multiplied by charge $(q * p)$ and in the bottom panel, 1D projection of m^2 is shown in the analysed momentum range of $0.2 < p_T < 2$ GeV/c. The protons and antiprotons are selected using m^2 cut of $0.6 < m^2 < 1.2$ GeV^2/c^4, in the rapidity range $1.1 < y < 2.1$ and momentum range $0.2 < p_T < 2.0$ GeV/c. The $y - p_T$ acceptance of proton and antiproton is shown in Fig 5.38, and the box in the plot shows the region of analysis.

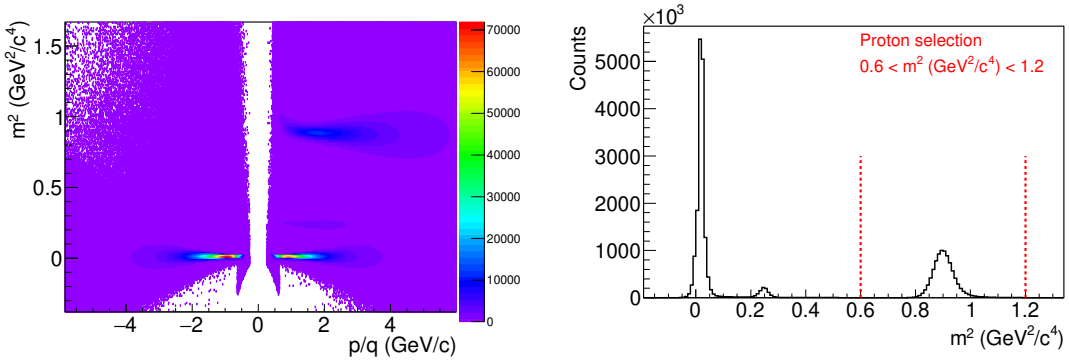

Figure 5.39: (Left Panel) Mass-squared vs Momentum/Charge. Protons(Antiprotons) are chosen using the cut $0.6 < m^2 < 1.2$ GeV^2/c^4. (Right Panel) 1D projection of m^2 in momentum range $0.2 < p_T < 2$ GeV/c.

RefMult

To avoid the autocorrelation, RefMult is measured using charged tracks with $m^2 <$ 0.4 GeV^2/c^4 within the pseudorapidity acceptance range ($1.5 < \eta < 3.8$). Fig 5.40 shows the RefMult distribution for the net-proton analysis for $E_{lab} = 10$ AGeV. The analysis is performed in 9 centrality classes : 0 - 5 %, 5 - 10 %, 10 - 20 %, 20 - 30 %, 30 - 40 %, 40 - 50 %, 50 - 60 %, 60 - 70 %, and 70 - 80 %. The number of events in each centrality class are listed in Table 5.1.

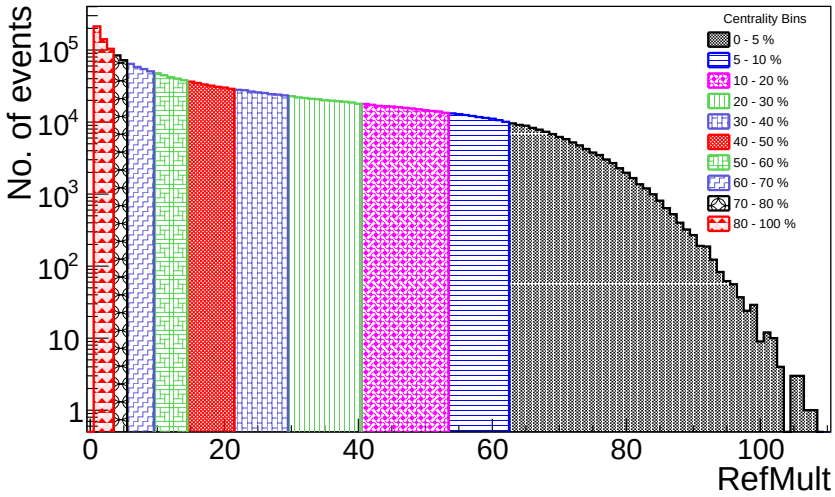

Figure 5.40: RefMult distribution in Net-proton analysis. The different coloured bands correspond to the different centrality classes. $0-5\%$ represents the most central collisions, while $70-80\%$ represents the most peripheral collisions used in our analysis.

Table 5.1: Number of events in each centrality class in net-proton analysis in Au-Au collision at $E_{lab} = 10$ AGeV.

Centrality (%)	**No. of Events**
0 - 5	110.4k
5- 10	105.8k
10 - 20	203.6k
20 - 30	223.5k
30 - 40	205.3k
40 - 50	226.7k
50 -60	212.1k
60 -70	227.6k
70 - 80	156.4k

5.3.4 Cumulants

Once the centrality classes are determined, the proton and antiproton distributions for each centrality class are measured. The multiplicity distribution of protons and antiprotons are shown in Fig. 5.41. The net-proton multiplicity distributions for all the centrality classes are shown in Fig. 5.42. The cumulants and central moments

upto 4^{th} order are calculated for net-proton multiplicity distributions using Eqn. 4.7. The first cumulant C_1 of net-proton distribution decreases as we go from central to peripheral.

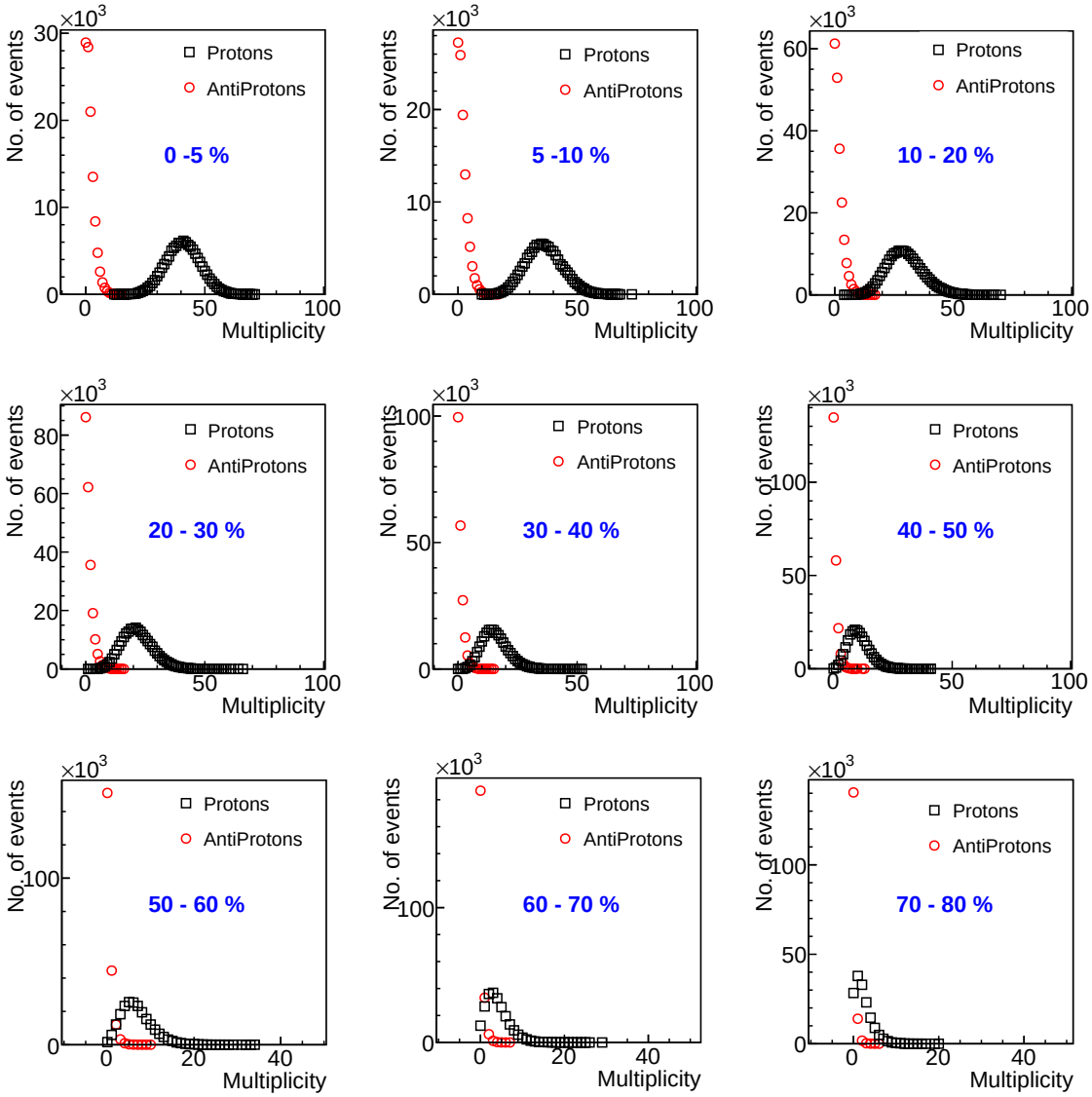

Figure 5.41: Multiplicity distribution of protons and antiprotons in different centrality classes in the η range 1.5-3.8, y range 1.1-2.1, p_T range 0.2 -2 GeV/c and E_{lab} = 10 AGeV.

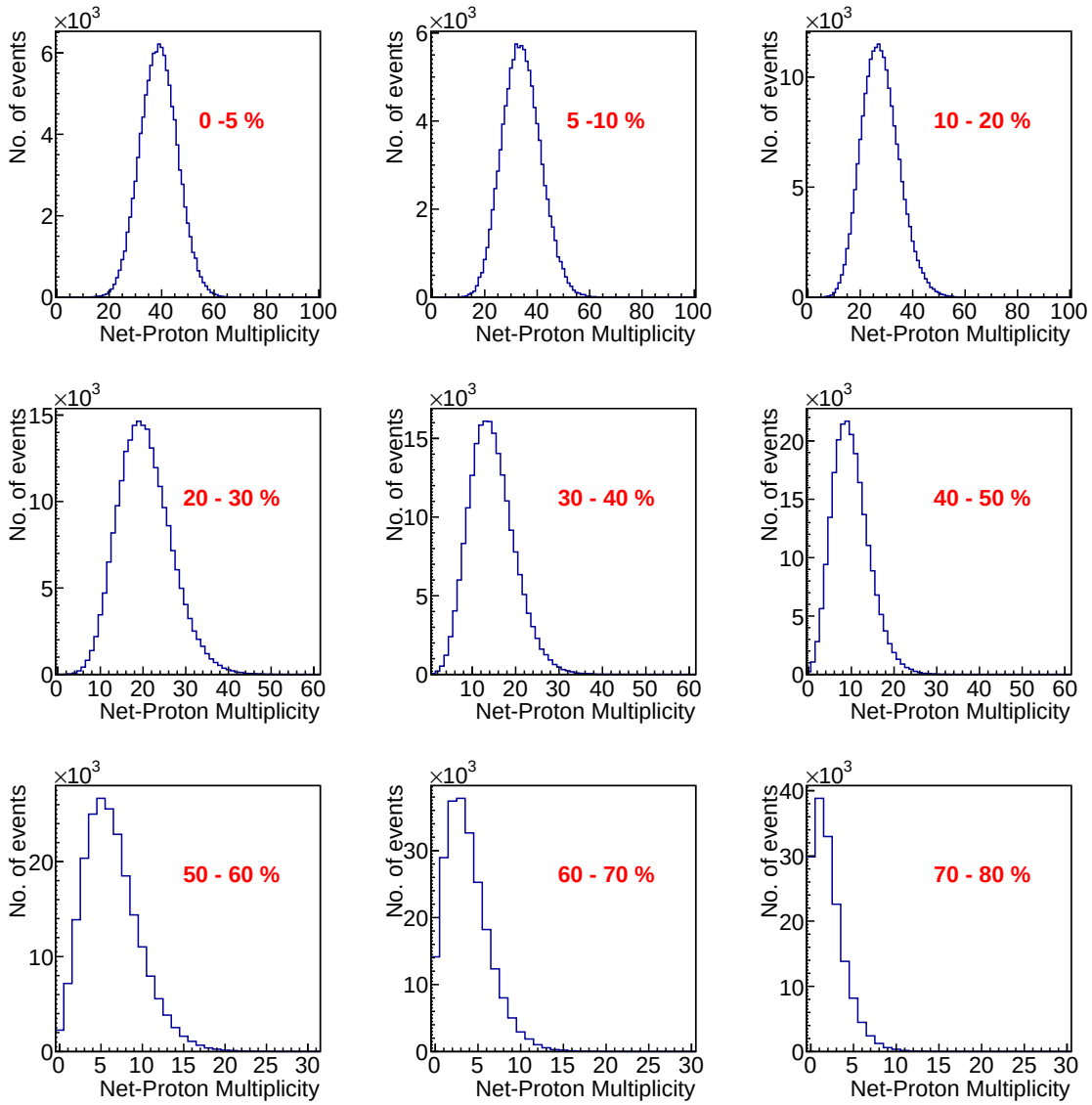

Figure 5.42: Multiplicity distribution of net-proton in different centrality classes in the η range 1.5-3.8, y range 1.1-2.1, p_T range 0.2 -2 GeV/c and $E_{lab} = 10$ AGeV.

Efficiency Correction Using Binomial Distribution

In real detectors, we don't have 100% efficiency of detection, which implies we lose out on the information from the actual collision. Thus, we need to estimate the effect of detector efficiency on the observable. Generally, the effect of efficiency (ϵ) can be modelled by a binomial distribution $B(N, \epsilon)$. The *binomial distribution* $B(N, \epsilon)$

is a discrete probability distribution of the number of successes in a sequence of N independent experiments for which the outcomes are success with probability ϵ and failure with probability $1 - \epsilon$.

Let the actual number of particles of a certain species produced event-by-event, N, have a distribution $\tilde{N}$. Let the efficiency of the detector be ϵ, and let the detector acceptance be modelled by $B(N, \epsilon)$. The distribution of the number of particles of that species which are detected, n is then given by:

$$P(n) = B(N, \epsilon)\tilde{N} \tag{5.5}$$

The Moment-Generating function is then given by

$$M(t) = (1 + (e^t - 1)\epsilon)^N \tag{5.6}$$

The moments can thus be calculated by evaluating the derivatives of $M(t)$ at $t = 0$. By inverting the equations for the moments of the distribution of the detected particles, we can thus get the moments of the distribution of the actual particles. The first four moments are listed below:

$$\begin{aligned}
\langle N \rangle &= \frac{\langle n \rangle}{\epsilon} \\
\langle N^2 \rangle &= \frac{\langle n^2 \rangle - \langle n \rangle(1-\epsilon)}{\epsilon^2} \\
\langle N^3 \rangle &= \frac{\langle n^3 \rangle - 3\langle n^2 \rangle(1-\epsilon) + \langle n \rangle(1-\epsilon)(2-\epsilon)}{\epsilon^3} \\
\langle N^4 \rangle &= \frac{\langle n^4 \rangle - 6\langle n^3 \rangle(1-\epsilon) + \langle n^2 \rangle(1-\epsilon)(11-7\epsilon) - \langle n \rangle(1-\epsilon)(6-(6-\epsilon)\epsilon)}{\epsilon^4}
\end{aligned} \tag{5.7}$$

where $< n^i >$ is the i^{th} order raw moment for the distribution of detected particles, and $< N^i >$ is the i^{th} order raw moment for the distribution of incident particles.

The new cumulants defined using these moments, should in principle give us the actual cumulants of (anti) proton multiplicity distributions. From Eqn. 4.9, we know that cumulants of independent distributions add up. Therefore, using the above

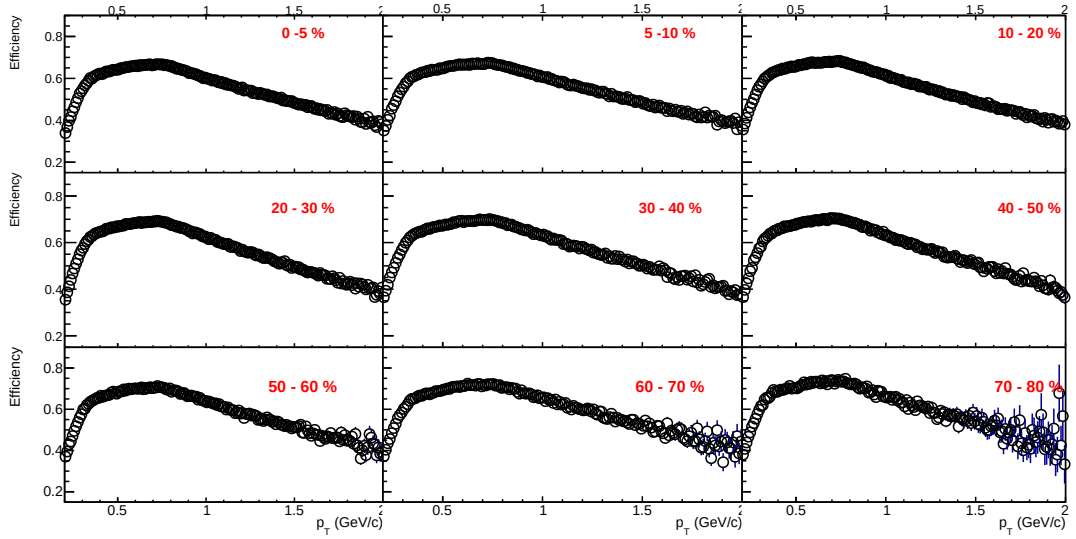

Figure 5.43: Efficiency of reconstruction of (anti)-protons vs transverse momentum (p_T) in different centrality bins in the η range 1.5-3.8, y range 1.1-2.1, p_T range 0.2 -2 GeV/c and E_{lab} = 10 AGeV. The error bars represent the statistical errors and are within the marker sizes for most cases.

formalism on both protons and antiprotons, we get the individual cumulants which are then subtracted to get the cumulants of net-proton.

For our analysis, we have defined efficiency in the following manner.

$$\text{Efficiency} = \frac{\text{Number of detected (anti)protons which are true (anti)protons}}{\text{Number of Incident (anti)protons}} \quad (5.8)$$

This definition also takes into account the purity of reconstruction of (anti)protons, however in our analysis, the purity is found to be over 90% in the centrality bins.

Fig 5.43 shows the efficiency of reconstruction of (anti)-protons as a function of the transverse momentum in the range $0.2 < p_T < 2$ GeV/c, for different centrality classes. The efficiency correctionn for the cumulants is done in each multiplicity bin, before it is bin width corrected. The efficiency corrected cumulants have been compared with the cumulants of the incident net-proton distribution in Fig. 5.44. There are visible disagreements between the incident and measured net proton cumulants, which suggests that this method might not be suited for our analysis.

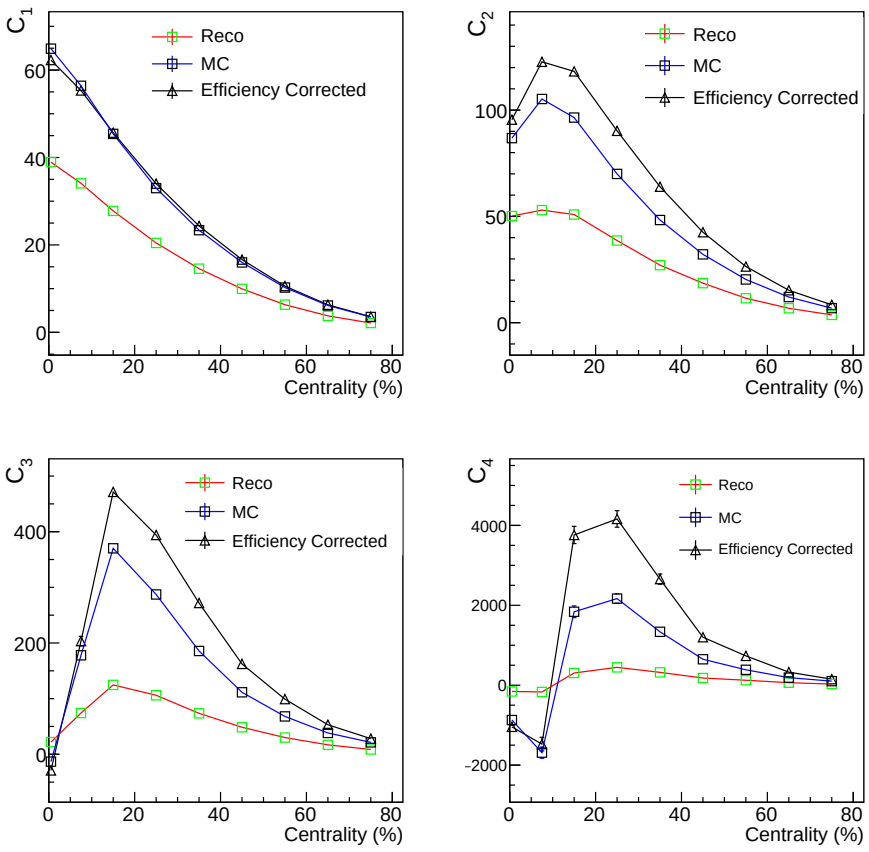

Figure 5.44: Net proton cumulants in various centrality classes efficiency correction using binomial distribution in the η range 1.5-3.8, y range 1.1-2.1, p_T range 0.2 -2 GeV/c and E_{lab} = 10 AGeV. For comparision, the cumulants of the incident net-proton distribution are also shown. The error bars represent the statistical errors and are within the marker size for most of the cases.

Efficiency Correction Using Unfolding

Since the modelling of the detector response using binomial distribution could not correct the cumulants obtained from simulation, a new method called *unfolding* has been used to correct for the detector responses. The unfolding algorithm has been implemented using the *RooUnfold* package [69]. There are two major algorithms for *unfolding* - Bayesian unfolding [69] and Singular Value Decomposition [70]. The Bayesian unfolding algorithm is descibed below [71]:

The procedure of Bayes unfolding can be explained by the causes C and the effects E. For our case, causes correspond to the true multiplicity values and effects to the measured multiplicity values which are affected by the inefficiencies. For $n(E)$ events with effect E due to several independent causes $(C_i, i = 1, 2, ..., n_C)$, the expected number of events assignable to each of the causes is given by the Bayes Theorem.

$$\hat{n}(C_i) = n(E)P(C_i|E) \tag{5.9}$$

where

$$P(C_i|E) = \frac{P(E|C_i)P(C_i)}{\sum_{l=1}^{n_C} P(E|C_l)P(C_l)} \tag{5.10}$$

Now if we observe that the outcome of a measurement has several possible effects $E_j(j = 1, 2, ..., n_E)$ for a given cause C_i, then the expected number of events to be assigned to each of the causes and only due to the observed events can be calculated to each effect by:

$$\hat{n}(C_i) = \sum_{j=1}^{n_E} n(E_j)P(C_i|E) \tag{5.11}$$

$P(C_i|E_j)$ is the probability that different causes C_i were responsible for the observed effect E_j and is calculated by Bayes theorem as:

$$P(C_i|E_j) = \frac{P(E_j|C_i)P_0(C_i)}{\sum_{l=1}^{n_C} P(E_j|C_l)P_0(C_l)} \tag{5.12}$$

where $P_0(C_i)$ are the initial probabilities.

If we take into account the inefficiency then the best estimate of the true number of events is given by

$$\hat{n}(C_i) = \frac{1}{\epsilon_i} \sum_{j=1}^{n_E} n(E_j)P(C_i|E); \epsilon_i \neq 0 \tag{5.13}$$

where ϵ_i is the efficiency of detecting the cause C_i in any of the possible effects. If $\epsilon_i = 0$, then $\hat{n}(C_i)$ is set to zero, since the experiment is not sensitive to the cause C_i.

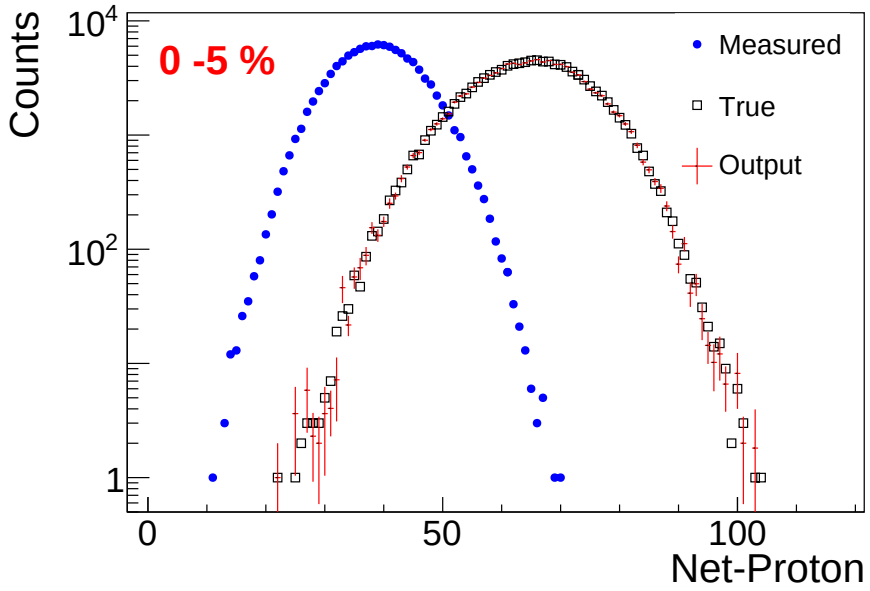

Figure 5.45: Measured, True, and Unfolded (using *RooUnfold*) distributions of net-proton multiplicity for 0 - 5 % centrality bin at E_{lab} = 10 AGeV. The error bars represent the statistical errors.

The above equation can be written in terms of unfolding or response matrix M_{ij} as

$$\hat{n}(C_i) = \sum_{j=1}^{n_E} M_{ij} n(E_j) \tag{5.14}$$

The response matrix M_{ij} is constructed using the number of detected net-proton and number of incident net-proton generated from a high statistics Monte Carlo sample.

In SVD method, the response matrix is constructed using the equation $\sum_j M_{ij} C_j = E_i$, where C and E are the same causes and effects as above. One then factorises an $m \times n$ dimensional M_{ij} into $M = USV^T$ where U is an $n \times n$ orthogonal matrix, V is an $n \times n$ orthogonal matrix, while S is an $m \times n$ matrix with non-negative diagonal elements and $S_{ij} = 0$ for $i \neq j$. This makes inverting M_{ij} easier as $M^{-1} = (USV^T)^{-1} = VS^{-1}U^T$, and one needs to only invert a diagonal matrix S. Thus, by inverting the first equation, one gets the matrix C_i, which is the true distribution.

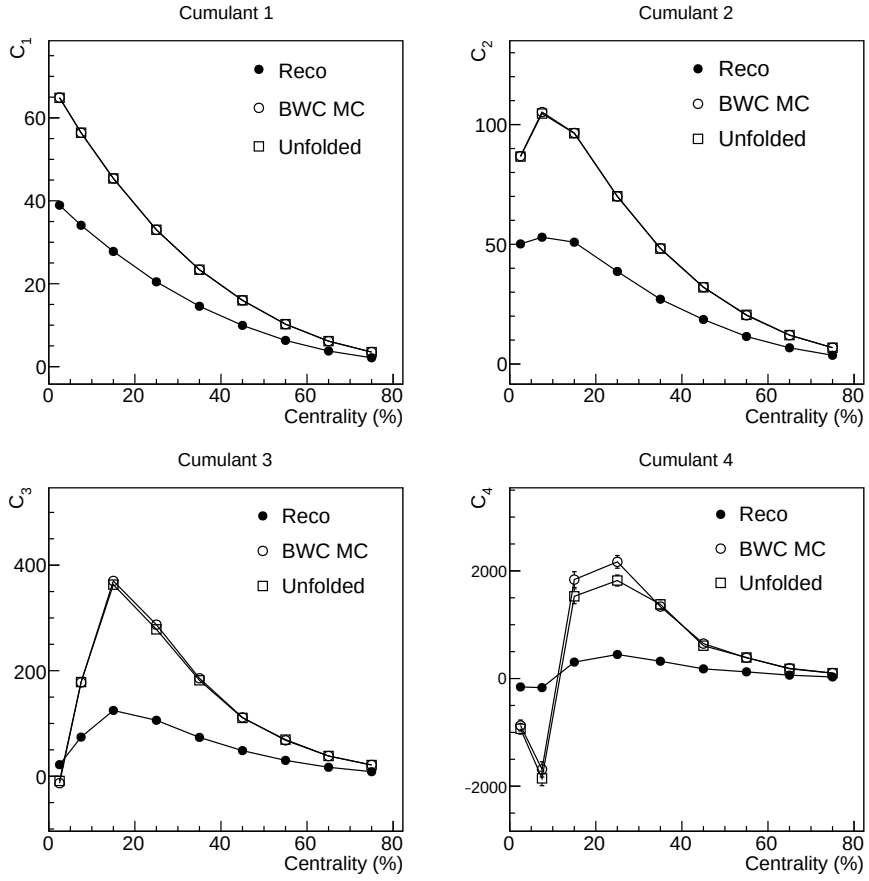

Figure 5.46: Net proton cumulants in various centrality classes after efficiency correction using unfolding in the η range 1.5-3.8, y range 1.1-2.1, p_T range 0.2 -2 GeV/c and $E_{lab} = 10$ AGeV. For comparision, the cumulants of the incident net-proton distribution are also shown. The error bars represent the statistical errors and are within the marker size for most cases.

We have used the Bayesian Unfolding technique for our analysis as it is the only method in the *RooUnfold* package which can unfold 2D distributions.

A result of unfolding net-proton distribution is presented in Fig. 5.45 for the most central (0 - 5 %) centrality class. Using unfolding, the calculated cumulants are presented in Fig. 5.46. This method is clearly better than efficiency correction using binomial acceptance, and the cumulants from the simulation match the cumulants from the model for $C_1, C_2, \& C_3$. C_4 from the simulation slightly deviates from the

real value for two centrality values, however, this may be removed by increasing statistics.

5.3.5 Net-Charge Fluctuation

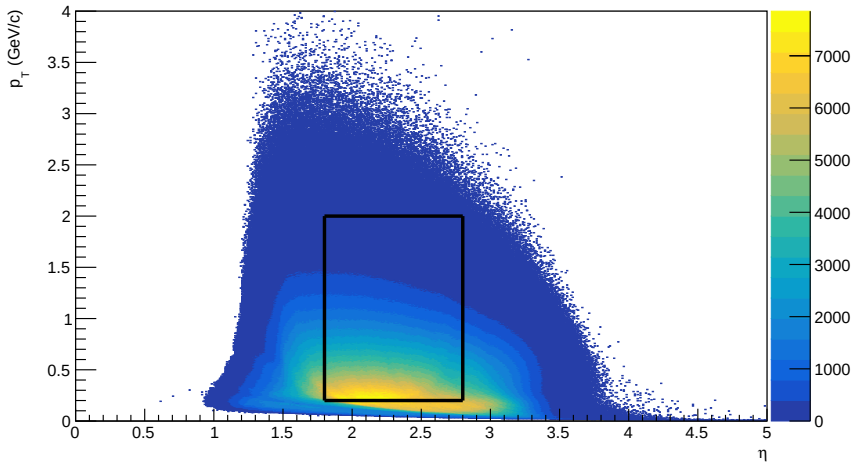

Figure 5.47: The distribution of pseudorapidity with transverse momentum p_T for all charged particles in the η range 1.5-3.8, p_T range 0.2 -2 GeV/c and $E_{lab} = 10$ AGeV. The tracks within the rectangular region have been chosen for analysis.

Particle Identification and Centrality Selection

The cuts used for the analysis of net-charge distribution have been discussed in section 5.3.2. Since all the charged particles in the pseudorapidity acceptance region are selected for analysis, we divide the pseudorapidity distribution into two distinct regions for analysis, and reference multiplicity (RefMult) selection. The RefMult is chosen in the range $1.5 < \eta < 1.8$ & $2.8 < \eta < 3.8$, while the particles in the range $1.8 < \eta < 2.8$ are used for net-charge fluctuation measurements. The relevant regions are shown in Fig. 5.48.

The RefMult is shown in Fig. 5.49. The number of events in each centrality class is listed in Table 5.2. The multiplicity distribution of positive and negative charges

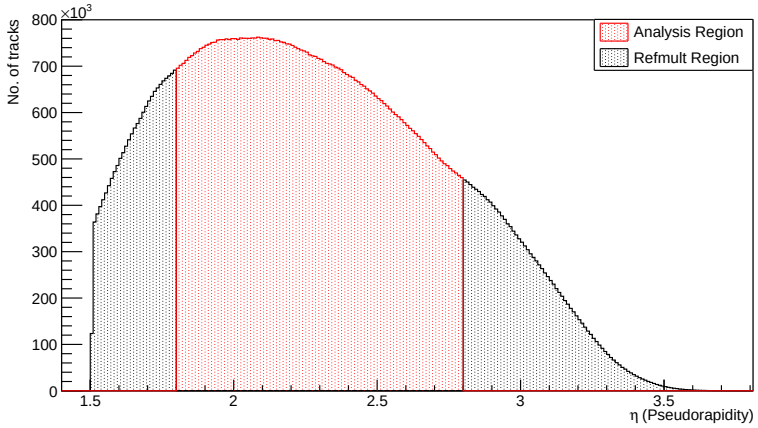

Figure 5.48: Pseudorapidity distribution of all charged particles in the η range 1.5-3.8, p_T range 0.2 -2 GeV/c, and E_{lab} = 10 AGeV. The *Refmult* region is used for constructing centrality classes.

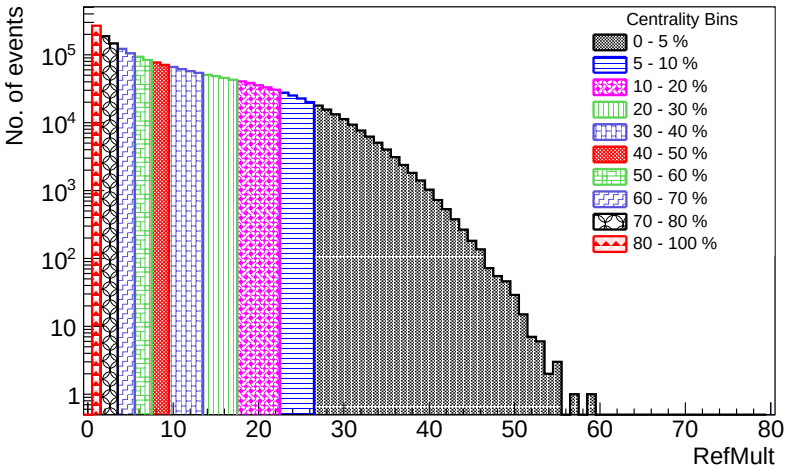

Figure 5.49: RefMult distribution for net-charge analysis in the η range 1.5-3.8, y range 1.1-2.1, p_T range 0.2 -2 GeV/c, and E_{lab} = 10 AGeV. $0-5\%$ represents the most central collisions, while $70-80\%$ represents the most peripheral collisions used in our analysis.

in every centrality bin is shown in Fig. 5.50. The net-charge multiplicity in every centrality bin is shown in Fig. 5.51. The efficiency corrected cumulants are shown in Fig. 5.52. There is excellent agreement between the cumulants calculated from simulation and those calculated from UrQMD.

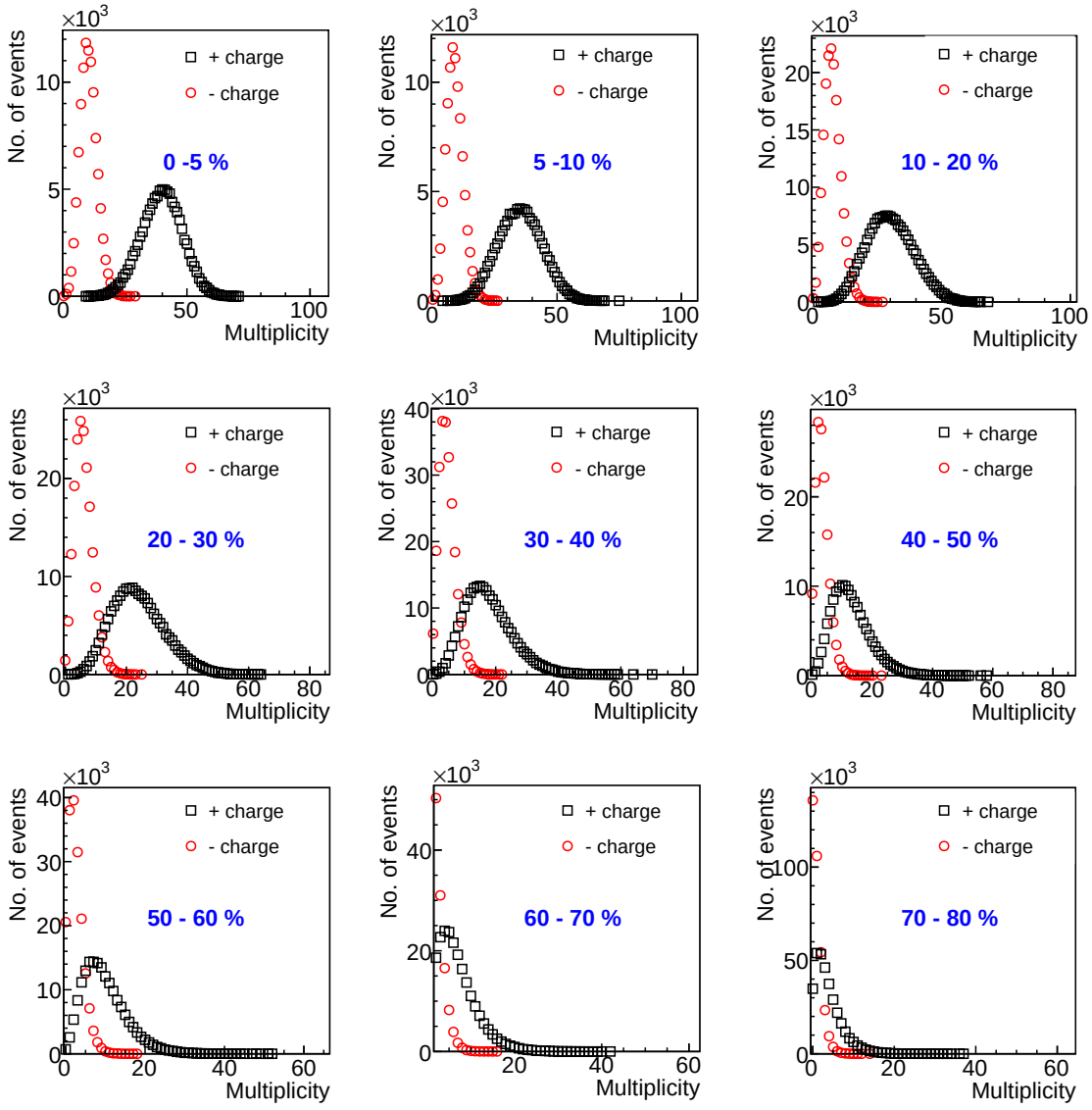

Figure 5.50: Multiplicity distribution of protons and antiprotons in different centrality classes in the η range 1.5-3.8, y range 1.1-2.1, p_T range 0.2 -2 GeV/c and $E_{lab} = 10$ AGeV.

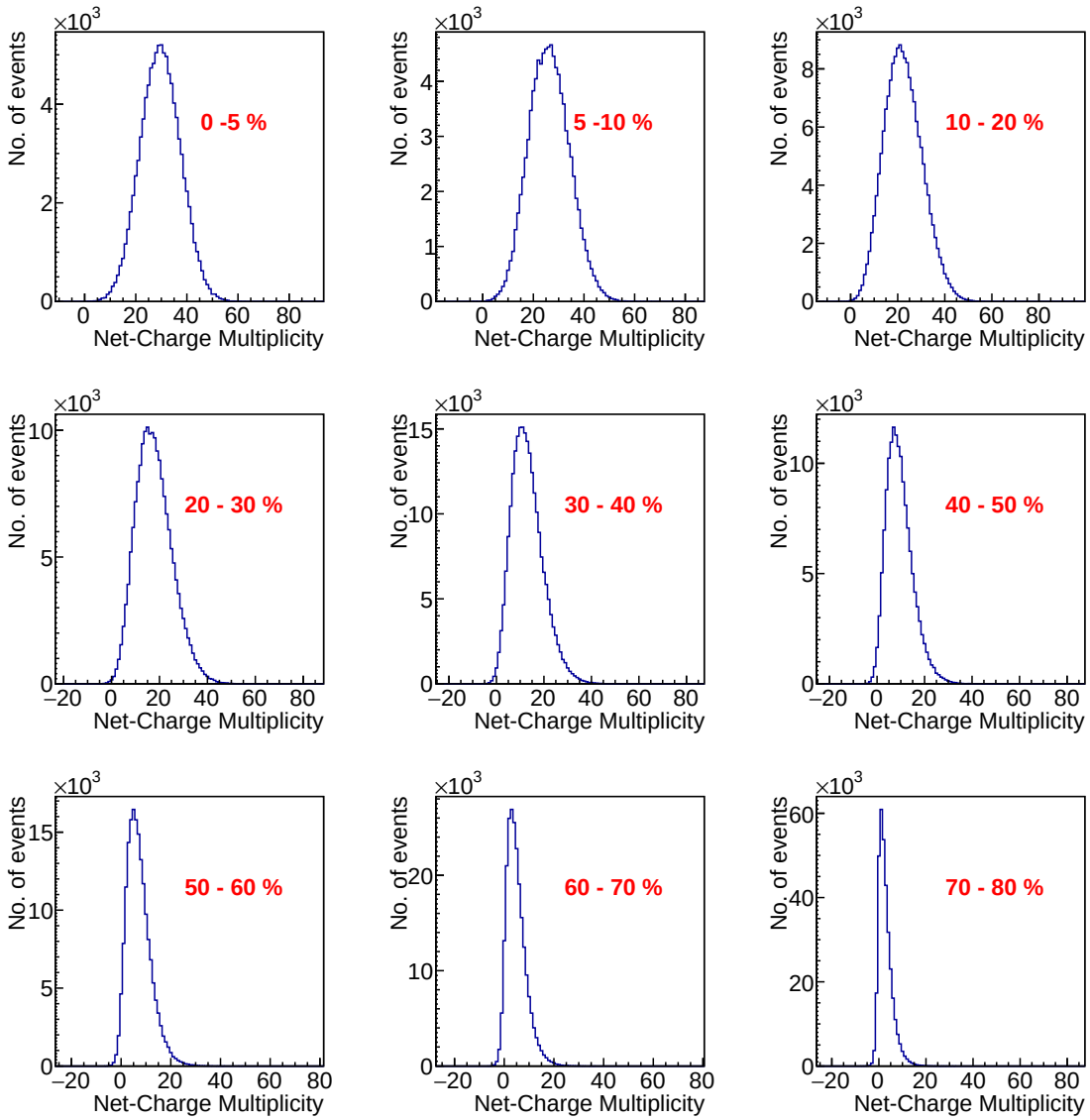

Figure 5.51: Multiplicity distribution of net-charge in different centrality classes in the η range 1.5-3.8, y range 1.1-2.1, p_T range 0.2 -2 GeV/c and $E_{lab} = 10$ AGeV.

Table 5.2: Number of events in each centrality bin in net-charge analysis for 2.78 million events of Au-Au collision at $E_{lab} = 10$ AGeV

Centrality (%)	**No. of Events**
0 - 5	102.6k
5- 10	95.6k
10 - 20	178.3k
20 - 30	187.8k
30 - 40	239.2k
40 - 50	148.0k
50 -60	177.4k
60 -70	227.6k
70 - 80	334.8k

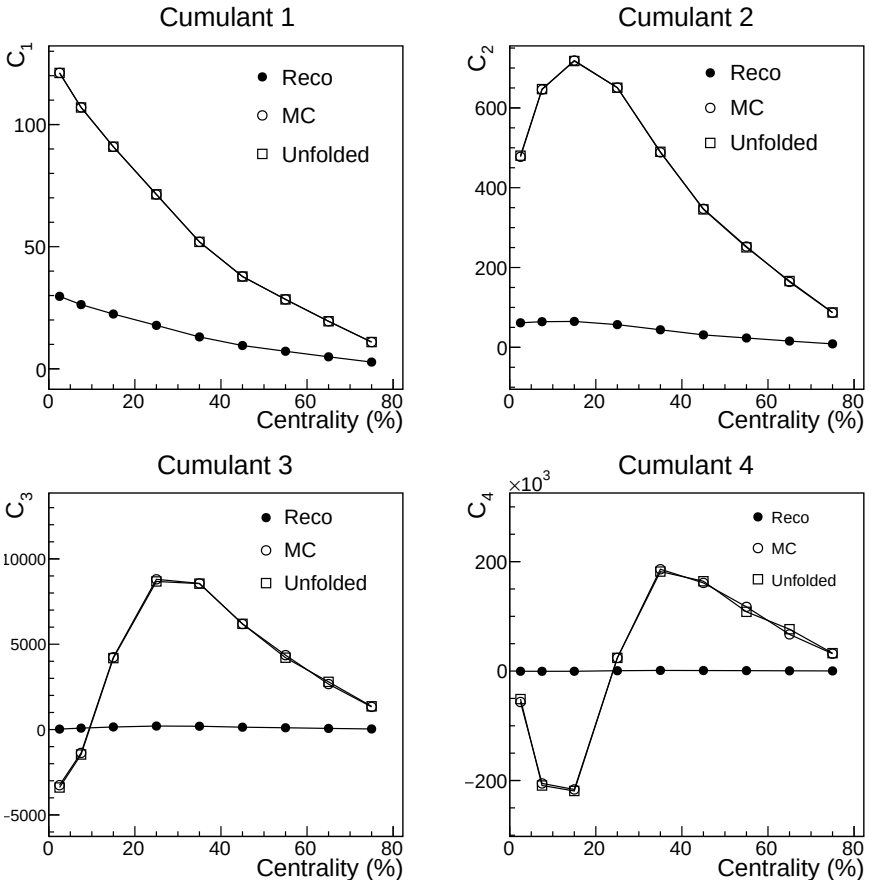

Figure 5.52: Net-charge fluctuations in various centrality classes before and after efficiency correction in the η range 1.5-3.8, y range 1.2-2.2, p_T range 0.2 -2 GeV/c, and $E_{lab} = 10$ AGeV. The error bars represent the statistical errors and are within the marker size.

5.3.6 Net-Kaon Fluctuations

Particle Identification

The kaons are selected using a m^2 cut of $0.18 < m^2 < 0.32$ GeV^2/c^4, in the rapidity range $1.1 < y < 2.1$ and momentum range $0.2 < p_T < 2.0$ GeV/c. The m^2 cut for identification of kaon is shown in Fig. 5.53.

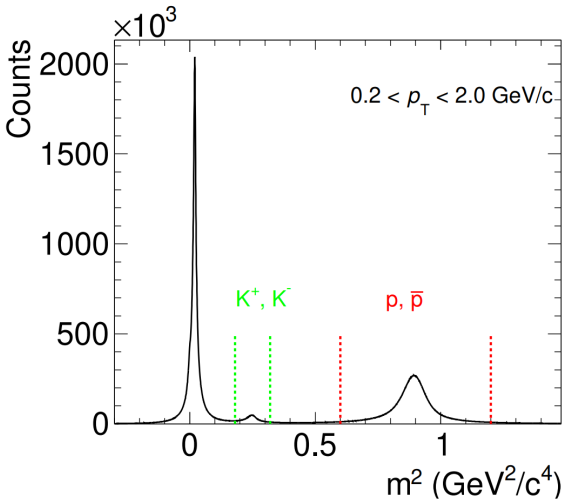

Figure 5.53: 1D projection of m^2 in the momentum range $0.2 < p_T < 2$ GeV/c. The m^2 cut for identifying kaons is shown.

Centrality Selection

To avoid autocorrelation, particles which have $m^2 < 0.15$ GeV^2/c^4 were chosen for *RefMult*. The *RefMult* distribution is shown in Fig. 5.54.

Table 5.3 contains the information about the number of particles in each centrality class. The net-kaon distribution at different centralities are shown in Fig. 5.55. The efficiency corrected cumulants are shown in Fig. 5.56. For C_3 and C_4, there is a small disagreement between the true value of C_3, C_4, and the ones obtained from unfolding for the most central collisions. This may be removed with increased statistics.

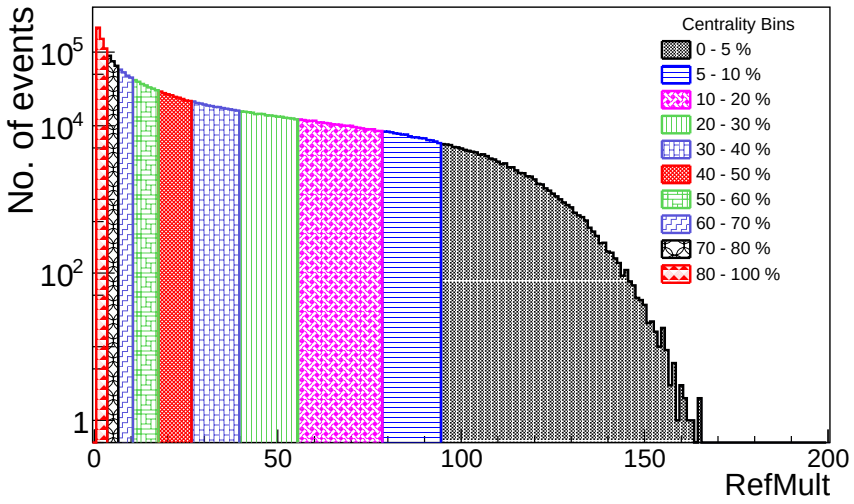

Figure 5.54: RefMult distribution for net-kaon analysis in the η range 1.5-3.8, y range 1.1-2.1, p_T range 0.2 -2 GeV/c, and E_{lab} = 10 AGeV. $0-5\%$ represents the most central collisions, while $70-80\%$ represents the most peripheral collisions used in our analysis.

Table 5.3: Number of events in each centrality bin in net-charge analysis for 2.78 million events of Au-Au collision at $E_{lab} = 10$ AGeV

Centrality (%)	**No. of Events**
0 - 5	113.8k
5- 10	115.0k
10 - 20	236.4k
20 - 30	223.0k
30 - 40	238.1k
40 - 50	225.2k
50 -60	249.1k
60 -70	203.9k
70 - 80	229.7k

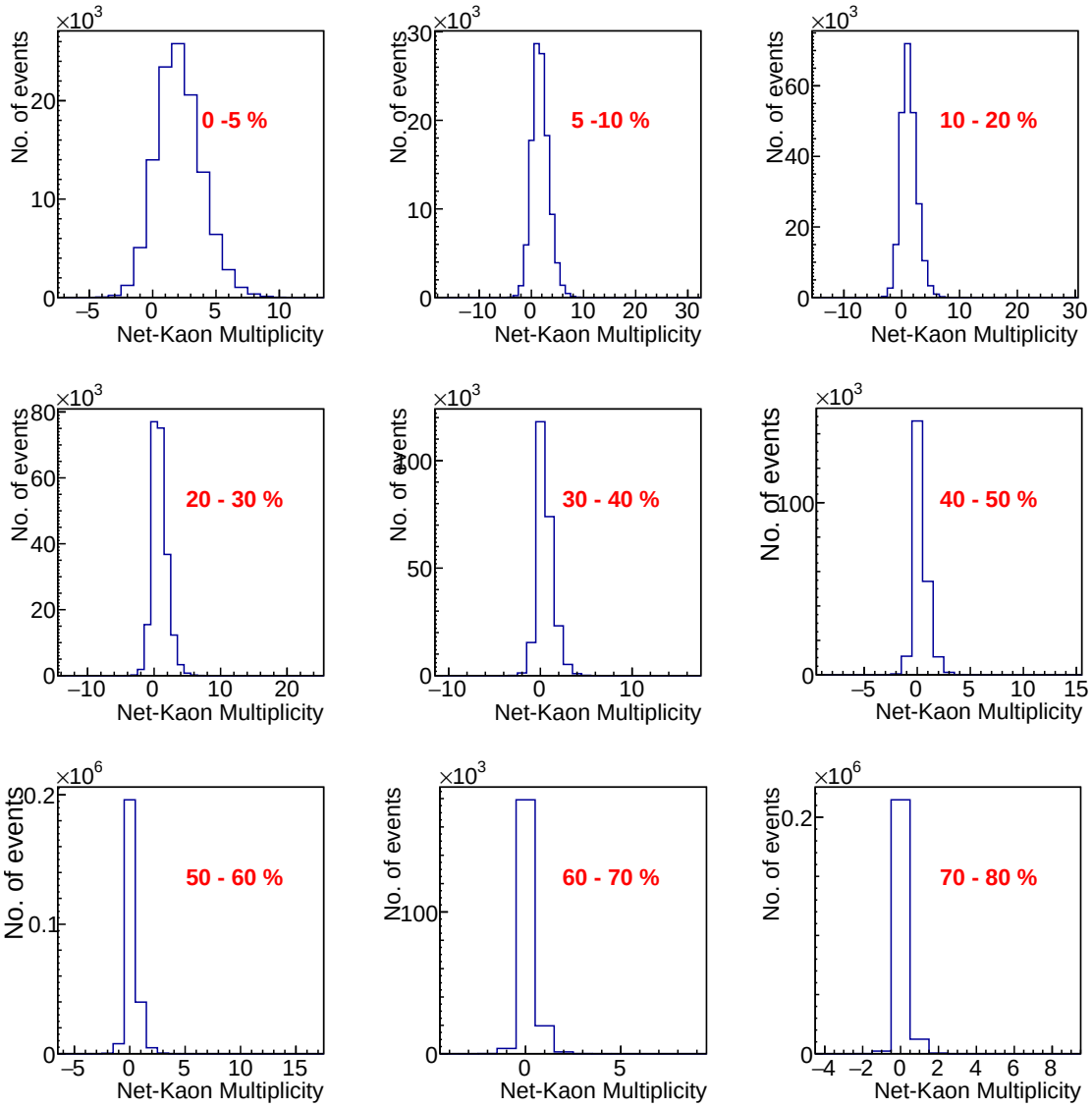

Figure 5.55: Multiplicity distribution of net-kaon in different centrality classes in the η range 1.5-3.8, y range 1.1-2.1, p_T range 0.2 -2 GeV/c and $E_{lab} = 10$ AGeV.

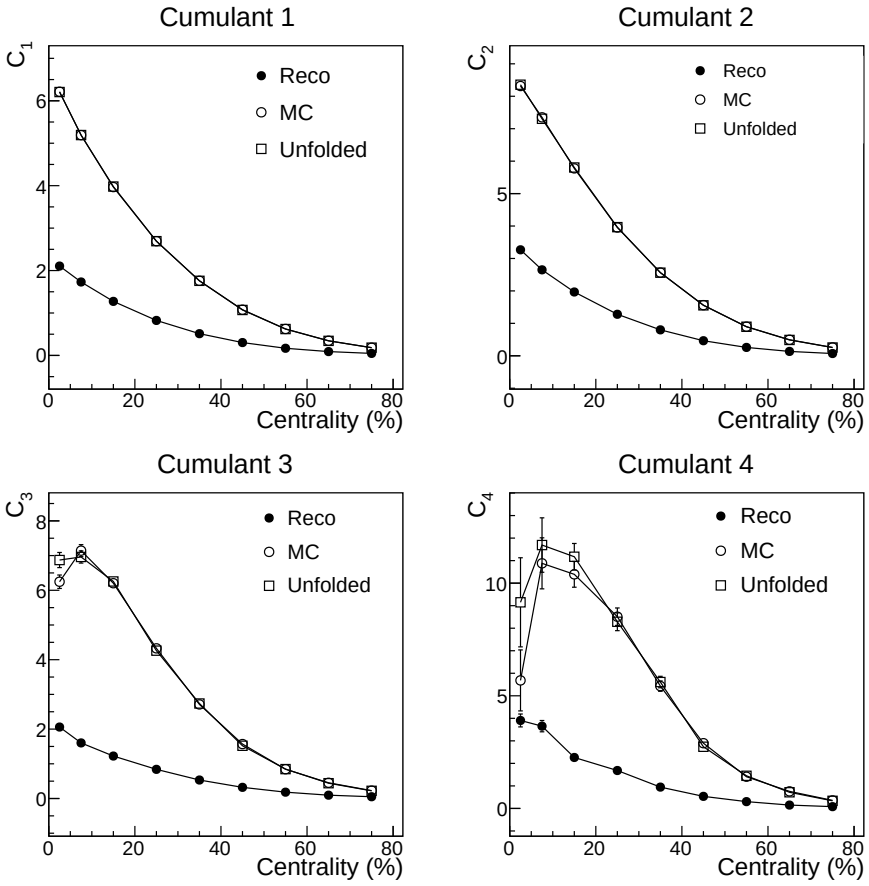

Figure 5.56: Net-kaon fluctuations in various centrality classes after efficiency correction using unfolding in the η range 1.5-3.8, y range 1.2-2.2, p_T range 0.2 -2 GeV/c, and E_{lab} = 10 AGeV. The error bars represent the statistical errors and are within the marker size for most cases.

5.3.7 Mixed Cumulants

For the mixed cumulants, the *RefMults* have already been defined. For net-proton, net-kaon mixed cumulants, we used the same *RefMult* as the one used for the analysis of net-kaon fluctuations, shown in Fig. 5.54. For mixed cumulants involving net-charge, we used the same *RefMult* as the one for the analysis of net-charge fluctuations, shown in Fig. 5.49.

Unfolding a 2D distribution

To calculate the efficiency-corrected mixed cumulants, we unfolded 2D-distributions for each pair of the conserved charges. This task is computationally intensive, as the algorithm used for unfolding scales as $O(N^4)$, where N is the number of bins of the distribution to be unfolded.

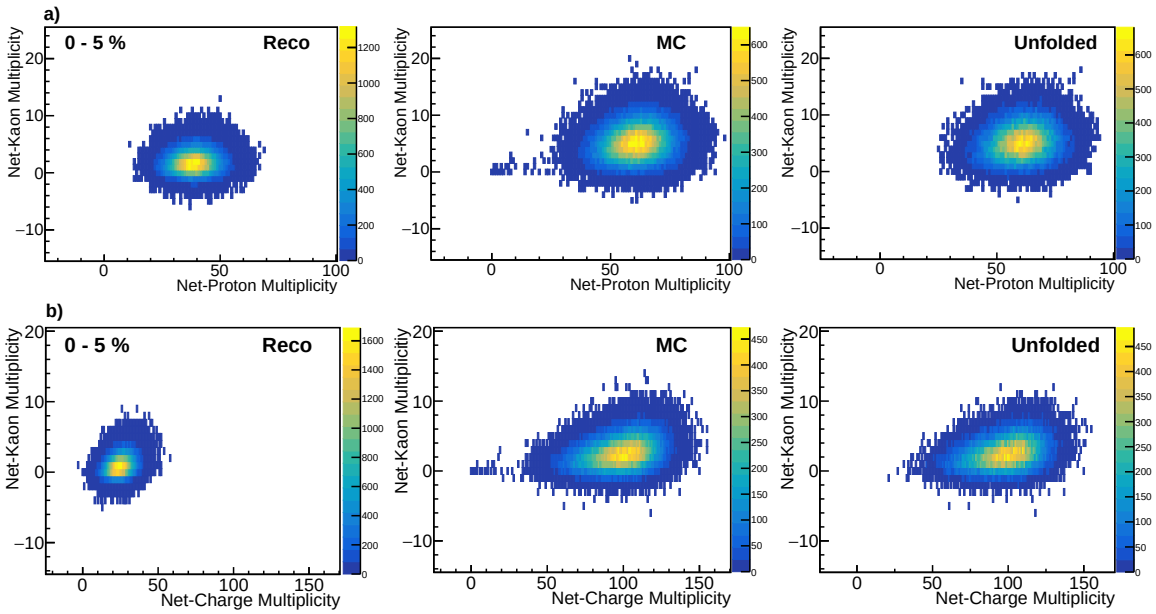

Figure 5.57: Unfolding of two 2D distributions for the most central (0 - 5%) centrality class. (a) Net-Proton, Net-Kaon 2D distribution. (b) Net-Charge, Net-Kaon 2D distribution. Left panel contains the measured distribution, middle panel contains the corresponding true distribution, and last panel contains the unfolded distribution.

In Fig. 5.57, we have shown the unfolding of 2 two-dimensional distributions. The first one is for calculating the mixed cumulant of net-proton and net-kaon distributions and the second one is for calculating the mixed cumulant of net-charge and net-kaon distributions. The second order mixed cumulants for net-proton, net-charge, and net-strangeness multiplicity distributions are shown in Figs. 5.58 - 5.60. There is excellent agreement between the cumulants dervied from UrQMD and the simulation.

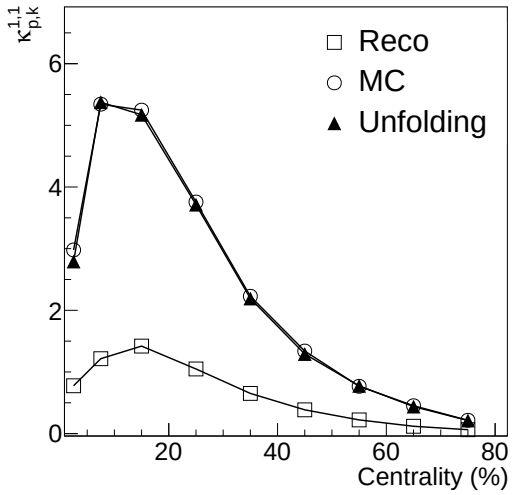

Figure 5.58: $\kappa_{p,k}$ as a function of centrality in the η range 1.5-3.8, y range 1.1-2.1, p_T range 0.2 -2 GeV/c, and E_{lab} = 10 AGeV. The error bars represent the statistical errors and are within the marker size.

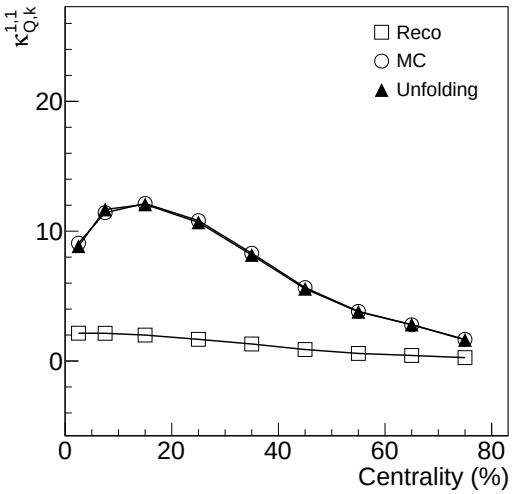

Figure 5.59: $\kappa_{Q,k}$ as a function of centrality in the η range 1.5-3.8, y range 1.1-2.1 (for kaons), p_T range 0.2 -2 GeV/c, and E_{lab} = 10 AGeV. The error bars represent the statistical errors and are within the marker size.

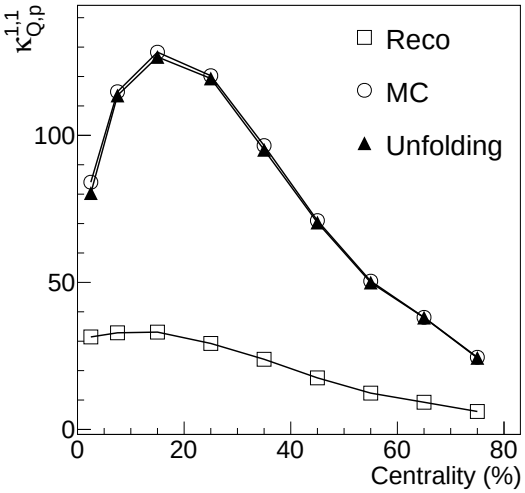

Figure 5.60: $\kappa_{Q,k}$ as a function of centrality in the η range 1.5-3.8, y range 1.1-2.1 (for (anti)protons), p_T range 0.2 -2 GeV/c, and E_{lab} = 10 AGeV. The error bars represent the statistical errors and are within the marker size.

Chapter 6

Summary and Outlook

In heavy-ion collision experiments, the study of event-by-event fluctuations is a powerful tool to characterize the thermodynamic properties of the hot and dense QCD matter. Experimentally, fluctuations of conserved quantities have been applied to probe the signature of the QCD phase transition and critical point in heavy-ion collisions. To understand the dependencies of these obervables, we have thus looked at the the first four cumulants of the net-proton, net-charge, and net-kaon multiplicity distributions at SIS energies ($E_{lab} = 4, 6, 8, 10$ AGeV), using a non-CP transport model UrQMD. Additionally, we have also looked at the second order mixed cumulants which are related to observables expected to show a rapid change during the transition of the system from de-confined to confined state.

We also studied the dependence of cumulants on centrality within the CBM detector setup. One aspect would be to look at these cumulants as function of varying rapidity acceptances. The challenge at the detector level is to get back the original particle distributions. To do that, we have looked at various effects which distort the original distributions like centrality bin width effect, and detector inefficiencies. We have used two methods for addressing detector inefficiencies, and pointed out the shortcoming of using the binomial acceptance to correct for such effects. We have also set up the unfolding method, and have used it to correct both diagonal and off-diagonal cumulants. Unfolding for the off-diagonal cumulants has its own challenges - the algorithm takes extremely long times to unfold distributions with many particles. Another step would be to figure out an efficient way to unfold 2D distributions.

References

[1] B. Friman, et al., The CBM Physics Book, Lect.Notes Phys. 814, Springer 2011.

[2] P. Giubellino, *Nucl. Phys. A*, **715**, 441 (2003).

[3] A. Aprahamian *et al.*,"Reaching for the horizon: The 2015 long range plan for nuclear science," INSPIRE-1398831.

[4] Y. Aoki et al, *Nature*, **443**, 675 (2006).

[5] S. Ejiri, *Phys. Rev. D*, **78**, 074507 (2008).

[6] K. Rajagopal and F. Wilczek, In *Shifman, M. (ed.): At the frontier of particle physics, vol. 3* 2061-2151 [hep-ph/0011333].

[7] M. A. Stephanov, K. Rajagopal and E. V. Shuryak, *Phys. Rev. Lett.* **81**, 4816 (1998).

[8] M. A. Stephanov, K. Rajagopal and E. V. Shuryak, *Phys. Rev. D* **60**, 114028 (1999).

[9] B. I. Abelev *et al.* [STAR Collaboration], *Phys. Rev. C* **81**, 024911 (2010).

[10] STAR Internal Note - SN0493, 2009.

[11] M. A. Stephanov, *Phys. Rev. Lett.* **102**, 032301 (2009).

[12] M. Cheng *et al.*, *Phys. Rev.* **D79**, 074505 (2009).

[13] M. A. Stephanov, *Phys. Rev. Lett.* **107**, 052301 (2011).

[14] S. Gupta, B. Mohanty, *Science*, **332**, 1525-1528 (6037).

[15] B. Berdnikov and K. Rajagopal, *Phys. Rev. D* **61**, 105017 (2000).

[16] L. Adamczyk et al. (STAR Collaboration), *Phys. Rev. Lett.*, **112**, 032302 (2014).

[17] L. Adamczyk et al. (STAR Collaboration), *Phys. Rev. Lett.*, **113**, 092301 (2014).

[18] L. Adamczyk et al. (STAR Collaboration), *Phys. Rev. B*, **785**, 551 (2018).

[19] L. Adamczyk et al. (STAR Collaboration), *arXiv:1903.05370v2* (2019).

[20] V. Koch, A. Majumder, and J. Randrup, *Phys. Rev. Lett.* **95**, 182301 (2005).

[21] R. V. Gavai, S. Gupta, *Phys. Rev. D* **73**, 014004 (2006).

[22] A. Bazavov *et al.*, *Phys. Rev. Lett.* **111**, 082301 (2013).

[23] V. Koch *et al.*, *Phys. Rev. Lett.* **95**, 182301 (2005).

[24] F. Karsch, *Nucl. Phys. A* **967**, 461 (2017).

[25] T. Ablyazimov, *Eur. Phys. J. A*, **53**, 60 (2017).

[26] J.M. Heuser, *Nuclear Physics A*, **830**, 563-566 (2009).

[27] C. Hohne *et al.*: Part V CBM Experiment. Lect. Notes Phys. 814, 849972 (2011).

[28] A. Malakhov, A. Shabunov, *GSI Report 2013*, `http://repository.gsi.de/record/109025`.

[29] R. Turchetta *et al.*, *Nucl. Instr.and Meth. A* **458** 677 (2001).

[30] M. Koziel *et al.*, *Nucl. Instr. and Meth. A* **732** 515 (2013).

[31] P. Senger and the Cbm Collaboration, *J. Phys.: Conf. Ser.*, **50** 357 (2006).

[32] J.M. Heuser et al., *GSI Report 2013-14*, `http://repository.gsi.de/record/54798`.

[33] C. Hohne, *GSI Report 2013-14*, `http://repository.gsi.de/record/65526`.

[34] C. Blume, *GSI Report 2018*, `http://repository.gsi.de/record/217478`.

[35] S. Chattopadhyay et al, *GSI Report 2015*, `http://repository.gsi.de/record/161297`.

[36] S. Herrmann, *GSI Report 2014*, `http://repository.gsi.de/record/109024`.

[37] F. Guber, I. Selyuzhenkov, *GSI Report 2015*, `http://repository.gsi.de/record/109059`.

[38] M. M. Aggarwal *et al.*, *Phys. Rev. Lett.*, **105**, 022302 (2010).

[39] J. Cleymans, H. Oeschler, K. Redlich, S. Wheaton, *Phys. Rev. C*, **73**, 034905 (2006).

[40] M. A. Stephanov, *International Journal of Modern Physics A*,**20**, 4387-4392 (2005).

[41] C.R. Allton, et. al., *Phys. Rev. D.* **71**, 054508 798 (2005).

[42] S. Borsanyi, Z. Fodor, J. N. Guenther, S. K. Katz, K. K. Szabo, A. Pasztor, I. Portillo, C. Ratti, *JHEP* **1810**, 205 (2018).

[43] M. D'Elia, G. Gagliardi, F. Sanfilippo, *Phys. Rev. D* **95**, 9, 094503 (2017).

[44] R. Bellwied, S. Borsanyi, Z. Fodor, S. D. Katz, A. Pasztor, C. Ratti, K. K. Szabo, *Phys. Rev. D* **92**, 11, 114505 (2015).

[45] A. Bazavov *et al.*, *Phys. Rev. D* **95**, 5, 054504 (2017).

[46] M. A. Stephanov, *Phys. Rev. Lett.* **102**, 032301 (2009).

[47] C. Athanasiou *et al.*, *Phys. Rev. D*, **82**, 074008 (2010).

[48] S. Zhang, Y. G. Ma, J. H. Chen, C. Zhong, *Adv. in High Energy Phys.*, **2015**, 460590, 2015.

[49] P. Braun-Munzinger, K. Redlich, J. Stachel, in *Quark Gluon Plasma 3* (Ref. [2]), pp. 491-599.

[50] A. Bazavov *et al.*, *Phys.Rev. D* **86**, 034509, (2012).

[51] Y. Hatta, M. A. Stephanov, *Phys. Rev. Lett.*, **91**, 102003 (2003).

[52] L. Adamczyk et al. (STAR Collaboration), *Phys. Rev. Lett.* **120**, 062301 (2018).

[53] `https://en.wikipedia.org/wiki/Skewness#/media/File:Negative_and_positive_skew_diagrams_(English).svg`

[54] https://en.wikipedia.org/wiki/Kurtosis#/media/File:Standard_symmetric_pdfs.png

[55] A. Pandav, D. Mallick and B. Mohanty, arXiv:1809.08892 [nucl-ex].

[56] A. DasGupta, Asymptotic Theory of Statistics and Probability, (Springer, Berlin) (2008).

[57] S.A Bass *et al.*, *Prog. Part. Nucl. Phys.*, **41**, 225-370 (1998).

[58] M. Bleicher *et al.*, *J. Phys. G*, **25**, 1859-1896 (1999).

[59] M. Miller, K. Reygers, S. J. Sanders, P. Steinberg, *Ann. Rev. Nucl. Part. Sci.*, **57**, 205 (2007).

[60] B. Abelev *et al.* arXiv:1301.4361v3 [nucl-ex].

[61] M. Mukherjee *et al.*, *J. Phys. G: Nucl. Part. Phys.*, **43**, 085102 (2016).

[62] P. Garg *et al.*, *J.Phys. G*, **40**, 055103 (2013).

[63] J. T. Balewski *et al.*, *Phys. Lett. B*, **420**, 211 (1998).

[64] C. Patrignani *et al.* (Particle Data Group), *Chin. Phys. C*, **40**, 100001 (2016).

[65] A. Andronic, P. Braun-Munzinger, J. Stachel, *Nucl. Phys. A*, **772**, 167 (2006).

[66] C. Zhou, J. Xu, X. Luo, F. Liu, *Phys. Rev. C*, **96**, 014909 (2017).

[67] https://redmine.cbm.gsi.de/projects/cbmroot/wiki/Wiki.

[68] P. Senger, N. Herrmann, *Nuclear Physics News*, **28**, 23-27 (2018).

[69] G. D'Agostini, *Nucl. Instrum. Meth. A*, **362**, 487 (1995).

[70] A. Hoecker, V. Kartvelishvili, *Nucl.Instrum.Meth.A*, **372**, 469-481,1996.

[71] P. Garg, D K Mishra, P K Netrakanti, A K Mohanty, B Mohanty, *J. Phys. G: Nuclear and Particle Physics*, **40**, 5, (2012).

Appendix A

(*run_mc.C*)

```
// ------------------------------------------------------------------------
//
// Macro for standard transport simulation using UrQMD input and GEANT3
//
// V. Friese   22/02/2007
//
// Version 2016-02-05
//
// For the setup (geometry and field), predefined setups can be chosen
// by the second argument. A list of available setups is given below.
// The input file can be defined explicitly in this macro or by the
// third argument. If none of these options are chosen, a default
// input file distributed with the source code is selected.
//
// ------------------------------------------------------------------------


void run_mc(Int_t nEvents = 2,
const char* setupName = "sis100_electron",
//                          const char* setupName = "sis100_debug",
//                          const char* setupName = "sis100_hadron",
//                          const char* setupName = "sis100_muon_jpsi",
//                          const char* setupName = "sis100_muon_lmvm",
const char* inputFile = "")
{

// ========================================================================
//          Adjust this part according to your requirements

// -----   Environment   --------------------------------------------------
TString myName = "run_mc";  // this macro's name for screen output
TString srcDir = gSystem->Getenv("VMCWORKDIR");  // top source directory
// ------------------------------------------------------------------------


// -----   In- and output file names   ------------------------------------
TString inFile = ""; // give here or as argument; otherwise default is taken
TString outDir  = "data/";
TString outFile = outDir + setupName + "_test.mc.root";
TString parFile = outDir + setupName + "_params.root";
```

```
TString geoFile = outDir + setupName + "_geofile_full.root";
// ------------------------------------------------------------------------


// --- Logger settings ----------------------------------------------------
TString logLevel     = "INFO";
TString logVerbosity = "LOW";
// ------------------------------------------------------------------------


// --- Define the target geometry -----------------------------------------
//
// The target is not part of the setup, since one and the same setup can
// and will be used with different targets.
// The target is constructed as a tube in z direction with the specified
// diameter (in x and y) and thickness (in z). It will be placed at the
// specified position as daughter volume of the volume present there. It is
// in the responsibility of the user that no overlaps or extrusions are
// created by the placement of the target.
//
TString  targetElement   = "Gold";
Double_t targetThickness = 0.025;  // full thickness in cm
Double_t targetDiameter  = 2.5;    // diameter in cm
Double_t targetPosX      = 0.;     // target x position in global c.s. [cm]
Double_t targetPosY      = 0.;     // target y position in global c.s. [cm]
Double_t targetPosZ      = 0.;     // target z position in global c.s. [cm]
Double_t targetRotY      = 0.;     // target rotation angle around the y axis [deg]
// ------------------------------------------------------------------------


// --- Define the creation of the primary vertex  -------------------------
//
// By default, the primary vertex point is sampled from a Gaussian
// distribution in both x and y with the specified beam profile width,
// and from a flat distribution in z over the extension of the target.
// By setting the respective flags to kFALSE, the primary vertex will always
// at the (0., 0.) in x and y and in the z centre of the target, respectively.
//
Bool_t smearVertexXY = kTRUE;
Bool_t smearVertexZ  = kTRUE;
Double_t beamWidthX   = 0.1;  // Gaussian sigma of the beam profile in x [cm]
Double_t beamWidthY   = 0.1;  // Gaussian sigma of the beam profile in y [cm]
// ------------------------------------------------------------------------


// In general, the following parts need not be touched
// ========================================================================


// -----    Timer   -------------------------------------------------------
TStopwatch timer;
```

```
timer.Start();
// ------------------------------------------------------------------------


// -----   Debug option   -------------------------------------------------
gDebug = 0;
// ------------------------------------------------------------------------


// -----   Remove old CTest runtime dependency file   ---------------------
TString depFile = Remove_CTest_Dependency_File(outDir, "run_mc" , setupName);
// ------------------------------------------------------------------------



// -----   Create simulation run   ----------------------------------------
FairRunSim* run = new FairRunSim();
run->SetName("TGeant3");              // Transport engine
run->SetOutputFile(outFile);          // Output file
run->SetGenerateRunInfo(kTRUE);       // Create FairRunInfo file
// ------------------------------------------------------------------------


// -----   Logger settings   ----------------------------------------------
FairLogger::GetLogger()->SetLogScreenLevel(logLevel.Data());
FairLogger::GetLogger()->SetLogVerbosityLevel(logVerbosity.Data());
// ------------------------------------------------------------------------


// -----   Load the geometry setup   --------------------------------------
std::cout << std::endl;
TString setupFile = srcDir + "/geometry/setup/setup_" + setupName + ".C";
TString setupFunct = "setup_";
setupFunct = setupFunct + setupName + "()";
std::cout << "-I- " << myName << ": Loading macro " << setupFile << std::endl;
gROOT->LoadMacro(setupFile);
gROOT->ProcessLine(setupFunct);
// You can modify the pre-defined setup by using
// CbmSetup::Instance()->RemoveModule(ESystemId) or
// CbmSetup::Instance()->SetModule(ESystemId, const char*, Bool_t) or
// CbmSetup::Instance()->SetActive(ESystemId, Bool_t)
// See the class documentation of CbmSetup.
// ------------------------------------------------------------------------


// -----   Input file   ---------------------------------------------------
std::cout << std::endl;
TString defaultInputFile = srcDir + "/input/urqmd.auau.10gev.centr.root";
if ( inFile.IsNull() ) {  // Not defined in the macro explicitly
if ( strcmp(inputFile, "") == 0 ) {  // not given as argument to the macro
inFile = defaultInputFile;
```

```
}
else inFile = inputFile;
}
std::cout << "-I- " << myName << ": Using input file " << inFile << std::endl;
// -------------------------------------------------------------------------


// -----   Create media   ---------------------------------------------------
std::cout << std::endl;
std::cout << "-I- " << myName << ": Setting media file" << std::endl;
run->SetMaterials("media.geo");       // Materials
// -------------------------------------------------------------------------


// -----   Create and register modules   ------------------------------------
std::cout << std::endl;
TString macroName = gSystem->Getenv("VMCWORKDIR");
macroName += "/macro/run/modules/registerSetup.C";
std::cout << "Loading macro " << macroName << std::endl;
gROOT->LoadMacro(macroName);
gROOT->ProcessLine("registerSetup()");
// -------------------------------------------------------------------------


// -----   Create and register the target   ---------------------------------
std::cout << std::endl;
std::cout << "-I- " << myName << ": Registering target" << std::endl;
CbmTarget* target = new CbmTarget(targetElement.Data(),
targetThickness,
targetDiameter);
target->SetPosition(targetPosX, targetPosY, targetPosZ);
target->SetRotation(targetRotY);
target->Print();
run->AddModule(target);
// -------------------------------------------------------------------------


// -----   Create magnetic field   ------------------------------------------
std::cout << std::endl;
std::cout << "-I- " << myName << ": Registering magnetic field" << std::endl;
CbmFieldMap* magField = CbmSetup::Instance()->CreateFieldMap();
if ( ! magField ) {
std::cout << "-E- run_sim_new: No valid field!";
return;
}
run->SetField(magField);
// -------------------------------------------------------------------------


// -----   Create PrimaryGenerator   ----------------------------------------
std::cout << std::endl;
```

```
std::cout << "-I- " << myName << ": Registering event generators" << std::endl;
FairPrimaryGenerator* primGen = new FairPrimaryGenerator();
// --- Uniform distribution of event plane angle
primGen->SetEventPlane(0., 2. * TMath::Pi());
// --- Get target parameters
Double_t tX = 0.;
Double_t tY = 0.;
Double_t tZ = 0.;
Double_t tDz = 0.;
if ( target ) {
target->GetPosition(tX, tY, tZ);
tDz = target->GetThickness();
}
primGen->SetTarget(tZ, tDz);
primGen->SetBeam(0., 0., beamWidthX, beamWidthY);
primGen->SmearGausVertexXY(smearVertexXY);
primGen->SmearVertexZ(smearVertexZ);
//
// TODO: Currently, there is no guaranteed consistency of the beam profile
// and the transversal target dimension, i.e., that the sampled primary
// vertex falls into the target volume. This would require changes
// in the FairPrimaryGenerator class.
// -------------------------------------------------------------------------

// Use the CbmUnigenGenrator for the input
CbmUnigenGenerator*  uniGen = new CbmUnigenGenerator(inFile);
primGen->AddGenerator(uniGen);
run->SetGenerator(primGen);
// -------------------------------------------------------------------------


// -----   Run initialisation   ----------------------------------------------
std::cout << std::endl;
std::cout << "-I- " << myName << ": Initialise run" << std::endl;
run->Init();
// -------------------------------------------------------------------------


// -----   Runtime database   ------------------------------------------------
std::cout << std::endl << std::endl;
std::cout << "-I- " << myName << ": Set runtime DB" << std::endl;
FairRuntimeDb* rtdb = run->GetRuntimeDb();
CbmFieldPar* fieldPar = (CbmFieldPar*) rtdb->getContainer("CbmFieldPar");
fieldPar->SetParameters(magField);
fieldPar->setChanged();
fieldPar->setInputVersion(run->GetRunId(),1);
Bool_t kParameterMerged = kTRUE;
FairParRootFileIo* parOut = new FairParRootFileIo(kParameterMerged);
parOut->open(parFile.Data());
rtdb->setOutput(parOut);
rtdb->saveOutput();
```

```
rtdb->print();
// ------------------------------------------------------------------------


// -----   Start run   ----------------------------------------------------
std::cout << std::endl << std::endl;
std::cout << "-I- " << myName << ": Starting run" << std::endl;
run->Run(nEvents);
// ------------------------------------------------------------------------


// -----   Finish   -------------------------------------------------------
run->CreateGeometryFile(geoFile);
timer.Stop();
Double_t rtime = timer.RealTime();
Double_t ctime = timer.CpuTime();
std::cout << std::endl << std::endl;
std::cout << "Macro finished successfully." << std::endl;
std::cout << "Output file is "    << outFile << std::endl;
std::cout << "Parameter file is " << parFile << std::endl;
std::cout << "Geometry file is "  << geoFile << std::endl;
std::cout << "Real time " << rtime << " s, CPU time " << ctime
<< "s" << std::endl << std::endl;
// ------------------------------------------------------------------------
```

Appendix B

(*run_reco.C*)

```
// ------------------------------------------------------------------------
//
// Macro for digitisation and reconstruction of MC events with standard settings
//
// "old", event-by-event simulation and reconstruction chain.
// For time-based simulation, look at run_digi_tb.C
// and run_reco_tb_digi.C and run_reco_tb_track.C.
//
// This macro combines digitisation and reconstruction by using the
// macro modules digitize.C and reconstruct.C.
//
// The input file (...mc.root) can be chosen directly in the macro (line 42).
// or through the third argument to the macro call.
// If neither is done, the standard input for the regular tests is used.
//
// V. Friese   24/02/2006
// Version     18/03/2017 (V. Friese)
//
// ------------------------------------------------------------------------


void run_reco(Int_t nEvents = 2,
const char* setupName = "sis100_electron",
const char* inputFile = "")
{

// ========================================================================
//          Adjust this part according to your requirements

// --- Logger settings ----------------------------------------------------
TString logLevel     = "INFO";
TString logVerbosity = "LOW";
// ------------------------------------------------------------------------


// -----   Environment   --------------------------------------------------
TString myName = "run_reco";  // this macro's name for screen output
TString srcDir = gSystem->Getenv("VMCWORKDIR");  // top source directory
// ------------------------------------------------------------------------
```

```
// -----   In- and output file names   -------------------------------------------
TString inFile = ""; // give here or as argument; otherwise default is taken
TString outDir  = "data/";
TString outFile = outDir + setupName + "_test.eds.root";  // Output file (reco)
TString parFile = outDir + setupName + "_params.root";    // Parameter file
// -------------------------------------------------------------------------------


// -----   Remove old CTest runtime dependency file   ----------------------------
TString depFile = Remove_CTest_Dependency_File(outDir, "run_reco" , setupName);
// -------------------------------------------------------------------------------


// -----   Load the geometry setup   ---------------------------------------------
std::cout << std::endl;
TString setupFile = srcDir + "/geometry/setup/setup_" + setupName + ".C";
TString setupFunct = "setup_";
setupFunct = setupFunct + setupName + "()";
std::cout << "-I- " << myName << ": Loading macro " << setupFile << std::endl;
gROOT->LoadMacro(setupFile);
gROOT->ProcessLine(setupFunct);
// You can modify the pre-defined setup by using
// CbmSetup::Instance()->RemoveModule(ESystemId) or
// CbmSetup::Instance()->SetModule(ESystemId, const char*, Bool_t) or
// CbmSetup::Instance()->SetActive(ESystemId, Bool_t)
// See the class documentation of CbmSetup.
// -------------------------------------------------------------------------------


// -----   Parameter files as input to the runtime database   --------------------
std::cout << std::endl;
std::cout << "-I- " << myName << ": Defining parameter files " << std::endl;
TList *parFileList = new TList();
TString geoTag;

// - TRD digitisation parameters
if ( CbmSetup::Instance()->GetGeoTag(kTrd, geoTag) ) {
TObjString* trdFile = new TObjString(srcDir + "/parameters/trd/trd_" + geoTag + ".dig
parFileList->Add(trdFile);
std::cout << "-I- " << myName << ": Using parameter file "
<< trdFile->GetString() << std::endl;
}

// - TOF digitisation parameters
if ( CbmSetup::Instance()->GetGeoTag(kTof, geoTag) ) {
TObjString* tofFile = new TObjString(srcDir + "/parameters/tof/tof_" + geoTag + ".dig
parFileList->Add(tofFile);
std::cout << "-I- " << myName << ": Using parameter file "
<< tofFile->GetString() << std::endl;
TObjString* tofBdfFile = new TObjString(srcDir + "/parameters/tof/tof_" + geoTag + "
```

```
parFileList->Add(tofBdfFile);
std::cout << "-I- " << myName << ": Using parameter file "
<< tofBdfFile->GetString() << std::endl;
}
// -------------------------------------------------------------------------

// In general, the following parts need not be touched
// ========================================================================


// ----    Timer    -------------------------------------------------------
TStopwatch timer;
timer.Start();
// -------------------------------------------------------------------------


// ----    Debug option    -------------------------------------------------
gDebug = 0;
// -------------------------------------------------------------------------


// ----    Input file    ----------------------------------------------------
std::cout << std::endl;
TString defaultInputFile = "data/";
defaultInputFile = defaultInputFile + setupName + "_test.mc.root";
if ( inFile.IsNull() ) {  // Not defined in the macro explicitly
if ( strcmp(inputFile, "") == 0 ) {  // not given as argument to the macro
inFile = defaultInputFile;
}
else inFile = inputFile;
}
std::cout << "-I- " << myName << ": Using input file " << inFile << std::endl;
// -------------------------------------------------------------------------


// ----    FairRunAna    ----------------------------------------------------

FairRunAna *run = new FairRunAna();
FairFileSource* inputSource = new FairFileSource(inFile);
run->SetSource(inputSource);
run->SetOutputFile(outFile);
run->SetGenerateRunInfo(kTRUE);
run->SetGenerateRunInfo(kTRUE);
Bool_t hasFairMonitor = Has_Fair_Monitor();
if (hasFairMonitor) FairMonitor::GetMonitor()->EnableMonitor(kTRUE);
// -------------------------------------------------------------------------


// ----    Logger settings    -----------------------------------------------
FairLogger::GetLogger()->SetLogScreenLevel(logLevel.Data());
FairLogger::GetLogger()->SetLogVerbosityLevel(logVerbosity.Data());
```

```
// -------------------------------------------------------------------------

// ----- Mc Data Manager   -------------------------------------------------
CbmMCDataManager* mcManager=new CbmMCDataManager("MCManager", 1);
mcManager->AddFile(inFile);
run->AddTask(mcManager);
// -------------------------------------------------------------------------

// -----    Digitisers    -------------------------------------------------
std::cout << std::endl;
TString macroName = gSystem->Getenv("VMCWORKDIR");
macroName += "/macro/run/modules/digitize.C";
std::cout << "Loading macro " << macroName << std::endl;
gROOT->LoadMacro(macroName);
gROOT->ProcessLine("digitize()");
// -------------------------------------------------------------------------


// -----    Reconstruction tasks   -------------------------------------------
std::cout << std::endl;
macroName = srcDir + "/macro/run/modules/reconstruct.C";
std::cout << "Loading macro " << macroName << std::endl;
gROOT->LoadMacro(macroName);
Bool_t recoSuccess = gROOT->ProcessLine("reconstruct()");
if ( ! recoSuccess ) {
std::cerr << "-E-" << myName << ": error in executing " << macroName
<< std::endl;
return;
}
std::cout << "-I-" << myName << ": " << macroName << " excuted successfully"
<< std::endl;
// -------------------------------------------------------------------------


// -----   Parameter database   --------------------------------------------
std::cout << std::endl << std::endl;
std::cout << "-I- " << myName << ": Set runtime DB" << std::endl;
FairRuntimeDb* rtdb = run->GetRuntimeDb();
FairParRootFileIo* parIo1 = new FairParRootFileIo();
FairParAsciiFileIo* parIo2 = new FairParAsciiFileIo();
parIo1->open(parFile.Data(),"UPDATE");
rtdb->setFirstInput(parIo1);
if ( ! parFileList->IsEmpty() ) {
parIo2->open(parFileList, "in");
rtdb->setSecondInput(parIo2);
}
// -------------------------------------------------------------------------


// -----   Run initialisation   --------------------------------------------
std::cout << std::endl;
```

```
std::cout << "-I- " << myName << ": Initialise run" << std::endl;
run->Init();
// ------------------------------------------------------------------------

rtdb->setOutput(parIo1);
rtdb->saveOutput();
rtdb->print();

// -----   Start run   ----------------------------------------------------
std::cout << std::endl << std::endl;
std::cout << "-I- " << myName << ": Starting run" << std::endl;
run->Run(0, nEvents);
// ------------------------------------------------------------------------


// -----   Finish   -------------------------------------------------------
timer.Stop();
Double_t rtime = timer.RealTime();
Double_t ctime = timer.CpuTime();
std::cout << std::endl << std::endl;
std::cout << "Macro finished succesfully." << std::endl;
std::cout << "Output file is " << outFile << std::endl;
std::cout << "Parameter file is " << parFile << std::endl;
std::cout << "Real time " << rtime << " s, CPU time " << ctime << " s"
<< std::endl;
std::cout << std::endl;
std::cout << " Test passed" << std::endl;
std::cout << " All ok " << std::endl;
// ------------------------------------------------------------------------
```